A Geochronological and Structural Analysis of the Nallamalai Fold Belt, S.E. India

Emma Alexander

Centre for Tectonics, Resources and Exploration

School of Earth and Environmental Sciences

The University of Adelaide, South Australia

emma.alexander@student.adelaide.edu.au

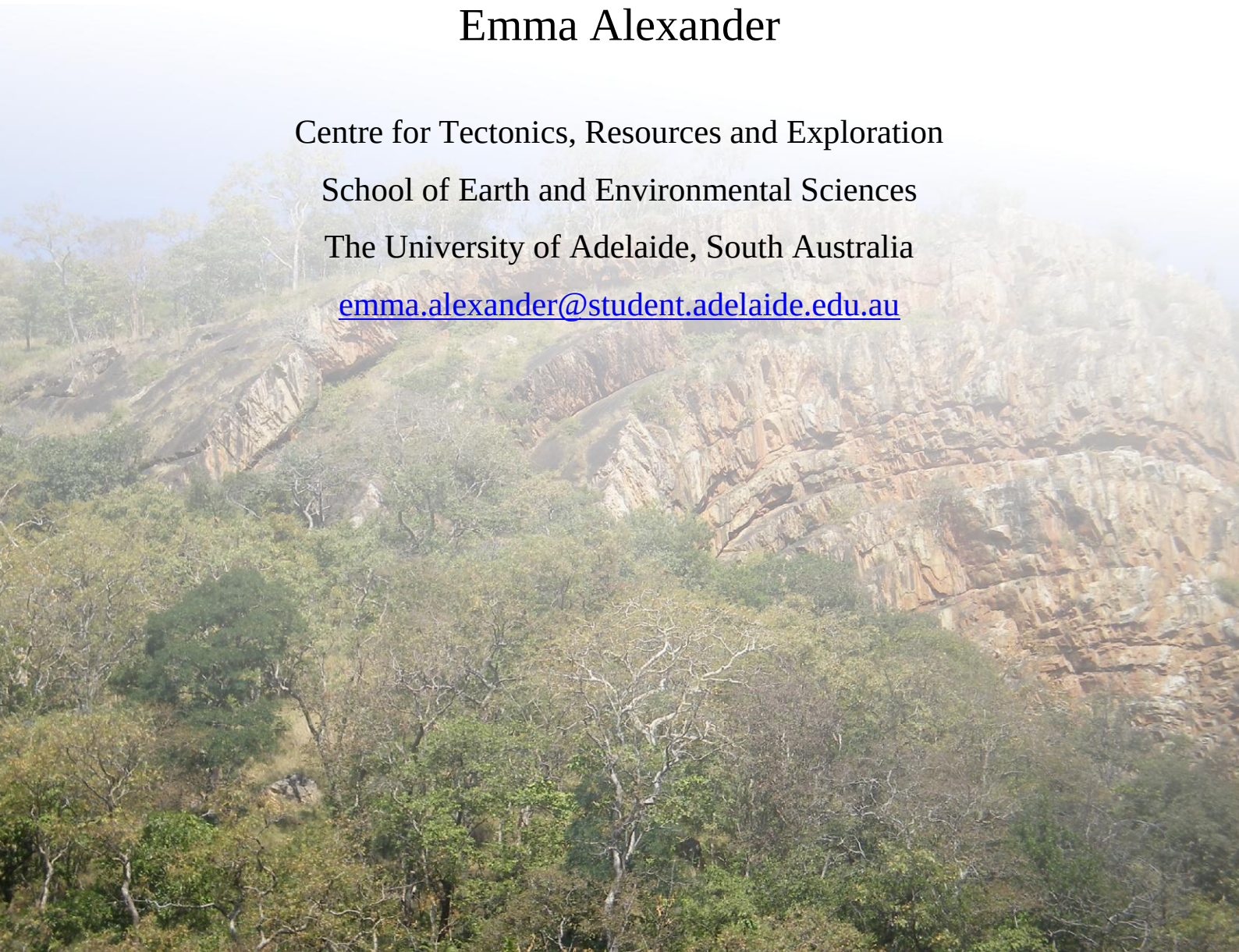

Contents

ABSTRACT

The Proterozoic sedimentary rocks of the Cuddapah Basin, South India, were deposited in diverse tectonic settings ranging from a rift basin to a foreland basin, and occur as several unconformity-bound sequences known as the Cuddapah Supergroup. The eastern half of this basin contains the heavily deformed quartzites and shales of the Nallamalai Fold Belt. A maximum depositional age of 1661 ± 20 Ma for the Nallamalai Group, along with recent age constraints of 1207 ± 22 Ma on the underlying Kurnool Group, defines the contact between the two as an east dipping thrust fault. Reconnaissance mapping coupled with broad scale ground truthing revealed a series of east dipping faults. These have been interpreted as attaching to a shallow décollement zone thought to propagate off the much larger, crustal scale thrust fault which forms the contact between the Nellore Schist Belt and the Nallamalai Fold Belt. Dominant detrital zircon age peaks were found to occur at ~1850 Ma and ~2500 Ma supporting the theory that the Nallamalai Group sediments were deposited as a foreland basin to the Eastern Ghats Belt. This is due to the ~1850 Ma detrital zircon population of the Nallamalai Group correlating geochemically with ~1850 Ma zircon population within the southern Eastern Ghats Belt. The age constraints placed on the north-south trending folds of the Nallamalai Fold Belt along with age constraints placed on the thrusting of Nallamalai rocks suggest original deformation occurred during the ~1640 – 1590 Ma collision between the southern Eastern Ghats Belt and the Dharwar Craton before further deformation at ~550 Ma which caused major detachment faulting within the Nallamalai Fold Belt during the amalgamation of Gondwana.

Key Words: Nallamalai Fold Belt, Cuddapah Basin, India, U-Pb Geochronology, Hf isotopes, Foreland basin, Gondwana, Supercontinents,

1.0 INTRODUCTION

The subcontinent of India plays host to a number of remarkably well preserved Proterozoic intracratonic basins (Figure 1a). These Proterozoic basins and their volcanic and sedimentary successions formed during the break-up of the Paleoproterozoic supercontinent Nuna (or Columbia), and the formation and break-up of the Late Mesoproterozoic-Early Neoproterozoic supercontinent Rodinia (eg. Chaudhuri *et al.* 2002; Saha & Chakraborty 2003).

The enigmatic Cuddapah Basin of Andhra Pradesh is one of India's largest intracratonic basins (French *et al.* 2008), covering approximately 44500 km^2 (Dasgupta *et al.* 2005). It contains one of the best preserved Paleo to Mesoproterozoic successions in the world. The sediments of the Cuddapah Basin are divided into two distinct groups; the Paleo to Mesoproterozoic Cuddapah Supergroup and the probable Neoproterozoic Kurnool Group (Figure 1b).

The stratigraphy of the Cuddapah Supergroup is complex and has been divided into four, unconformity- or fault-bound, stratigraphic divisions: from presumed oldest to youngest these are, the Papaghani Group, the Chitravati Group, the Nallamalai Group and the Srisailam Formation (Figure 2, eg. King 1872; Chatterjee & Bhattacharji 2001; Chaudhuri *et al.* 2002; Dasgupta & Biswas 2006; Ramakrishnan & Vaidyanadhan 2008). However, age relationships between these divisions are not always clear.

The Nallamalai Group is preserved only in the east of the Cuddapah Basin and is in fault-contact with all other stratigraphic divisions, making its stratigraphic position unclear. The Nallamalai Group is comprised of two formations, the older Bairenkonda Formation and the younger Cumbum Formation. These form a deformed

sedimentary succession (the Nallamalai Fold Belt - NFB) of unknown stratigraphic thickness that fills a basin with a seismically-defined base ~12km deep (Kailasam 1976) adjacent to the southern Eastern Ghats orogen (Figure 3).

There have been few studies that use modern dating procedures, such as U-Pb detrital zircon geochronology, to further constrain the timing of events from the less reliable Rb-Sr and K-Ar whole rock geochronology done in earlier studies. Furthermore, a detailed cross-section has not been attempted across the basin and through the NFB, as constraints on where the Nallamalai Group sits in relation to the rest of the basin are poor. Along with this, detailed structural mapping is made hard by the large study area and lack of accessibility.

A structural analysis on the NFB, using large scale field mapping accompanied by satellite image interpretation, is conducted with the aim to place robust constraints on the relationship between the Nallamalai sub-basin and other sub-basins of the Cuddapah Supergroup, despite previously mentioned limitations. Along with this Laser Ablation Inductively Coupled Plasma Mass Spectrometer (LA-ICPMS) U-Pb zircon geochronology, LA-ICPMS multicollector Hf isotope analysis, Rare Earth Element (REE) chemistry and Ti-in-zircon thermometry of the Nallamalai Group sediments is utilised to investigate the age and evolution of the Nallamalai sub-basin.

2.0 GEOLOGICAL SETTING

2.1 Regional Setting

The NFB is situated in the eastern half of the Cuddapah Basin in Andrah Pradesh, India. The Cuddapah Basin unconformably overlies the Archean Dharwar Craton that outcrops at the western border of the basin. To the east, the Cuddapah Basin is adjacent to the high-grade rocks of the Eastern Ghats Belt (EGB) (Figure 1a).

2.1.1 DHARWAR CRATON

The Dharwar Craton is situated in southwest India (Figure 1a). It is bound to the west by the Arabian Sea, to the east by the high grade EGB, to the south by the Southern Granulite Terrane, and to the north by Tertiary sediments and the Cretaceous Deccan Traps.

The Dharwar Craton is divided into the West Dharwar Craton (WDC) and the East Dharwar Craton (EDC), defined by major differences in lithology and age of the rock units (Meert *et al.* 2010). The base of the WDC is known as the Peninsular Gneiss Complex - an Early to Middle Archean (3.4–3 Ga) tonalitic-trondhjemitic-granodioritic (TTG) basement (Friend & Nutman 1991). Jayananda et al. (2008) describes three generations of volcano-sedimentary greenstone granite sequences within the WDC: 1) the Sargur Group (3.3-3.1 Ga) consisting of narrow, high-grade belts of greenstone-type volcanosedimentary sequences; 2) the Dharwar Supergroup (2.9-2.6 Ga) a low-grade volcanosedimentary sequence, and; 3) calc-alkaline to high potassic granitoids (2.6-2.5 Ga).

The EDC is composed of a series of parallel, N-S trending plutonic belts termed the Dharwar Batholith. Jayananda et al. (2000) constrain the age of emplacement of the Dharwar Batholith to the Late Archean (2.7–2.5 Ga). The EDC is also unconformably overlain by a number of Proterozoic-aged sedimentary basins, the largest being the Cuddapah Basin (Fig.1; Ramakrishnan & Vaidyanadhan 2008).

2.1.3 EASTERN GHATS BELT

The EGB is a Proterozoic granulite facies terrain that extends for ~1000 km along the east coast of southern Peninsular India (Figure 1). It is bordered to the north by the Archean rocks of the Singhbhum Craton, to the east by the Cuddapah Basin and

underlying Dharwar Craton, and is covered to the south and east by Tertiary alluvial plains and the Bay of Bengal.

Dobmeier and Raith (2003) have divided the belt into four provinces within two major orogens based on isotope and structural data. The four subdivisions are termed the Krishna Province of the Krishna Orogen; the Jeypore Province with an undefined orogenic event, and; the Rengali and Eastern Ghats Province of the Eastern Ghats Orogen. It is suggested that each province has its own distinct geological history. The Krishna Province shares its western border with the eastern side of the Cuddapah Basin and NFB making it of particular significance to this project.

The Krishna Province is comprised of the Ongole Domain granulites and the low- to medium-grade Nellore-Khammam Schist Belt. This schist belt can be further divided, along strike, into the Khammam Schist Belt in the north and the Nellore Schist Belt (NSB) in the south that have been directly thrust west over the NFB. Felsic magmatism has been dated within the Nellore-Khammam Schist Belt at 1868 ± 6 Ma and 1771 ± 8 Ma (Vasudevan *et al.* 2003). Final cooling of the schist belt in Neoproterozoic times is indicated by K-Ar muscovite ages of ~806 Ma (Gosh *et al.* 1994). The NSB further records a low-grade metamorphic overprint at 501–474 Ma (Dobmeier *et al.* 2006).

The depositional age of the Ongole Domain granulites is largely unconstrained, though felsic plutonic rocks have been dated at ~1.72 Ga (Dobmeier & Raith 2003). A major ultrahigh-temperature (UHT) metamorphic event is thought to have occurred at ~1.61 Ga, with overprinting at 1.45-1.35 Ga and further over printing at 500 Ma (Dobmeier & Raith 2003); presumably due to reworking of sediments during the amalgamation of the supercontinent Gondwana.

2.1.2 CUDDAPAH BASIN

The crescent shaped Cuddapah Basin covers approximately 44500 km^2 (Dasgupta *et al.* 2005). The basin is 440 km long and has a maximum width of 200 km in the middle (Kalpana *et al.* 2010). Deep seismic sounding profiles within the Cuddapah Basin indicate a total thickness of sediments of 5 to 8 km with a maximum of 10 km in the eastern part (Kailasam 1976).

The sediments of the Cuddapah Basin are divided into two distinct groups; the Paleo to Mesoproterozoic Cuddapah Supergroup and the probable Neoproterozoic Kurnool Group. The Cuddapah Supergroup is present throughout the entire basin, whilst the Kurnool Group is concentrated in the western portion of the basin.

It is widely agreed that prolonged, intermittent sedimentation within the Cuddapah Basin caused numerous unconformities within the Cuddapah Supergroup; essentially dividing it into four sequences (Figure1b, King 1872; Crawford & Compston 1973; Chalapathi Rao *et al.* 1996; Dasgupta *et al.* 2005). The four sequences are termed the Papaghani, the Chitravati and the Nallamalai groups and the Srisailam Formation. These four sequences are thought to represent separate sub-basins (Dasgupta *et al.* 2005). The three groups are further broken down into several formations with the Srisailam Formation sitting at the top of the Cuddapah Supergroup. Figure 2 outlines the stratigraphy of the Cuddapah Basin along with the previously known and proposed constraints on the age of deposition.

The evolution of the Cuddapah Basin is not well constrained and is still highly debated. Several models have been proposed as to the initiation and subsequent formation of the basin. One model proposes initiation as a rift basin during the break-up of the Paleoproterozoic supercontinent Columbia at ~1.9 Ga (Mishra 2011). The

basin then evolved into a foreland basin due to continent-continent collision involving the Cuddapah Basin and the EGB at ~1.6 Ga (Dasgupta & Biswas 2006; Manikyamba *et al.* 2008). The evolution of the basin into a foreland basin is suggested largely because of the overall deepening of the basin to the east – towards the Eastern Ghats Orogen.

Other models include: 1) The Cuddapah Basin as a peripheral foreland basin formed during eastward dipping subduction of the Dharwar Craton (Singh & Mishra 2002), and 2) the basin was formed due to a mantle induced thermal trigger (Chatterjee & Bhattacharji 2001).

2.2 Study Area

2.2.1 THE NALLAMALAI FOLD BELT

The NFB is an arcuate fold and thrust belt that is approximately 400 km in length. It is currently situated structurally at the top of the Cuddapah Supergroup (Saha 2002; Saha & Chakraborty 2003). However, although it is usually listed as being younger than the Papaghani and Chitravati groups, convincing constraints on the stratigraphic relationship between these groups are lacking. The Nallamalai Group is divided into the underlying Bairenkonda Quartzite (dominated with quartz-rich arenites) and the overlying Cumbum Formation (consisting of interbedded sandstones and shales). Some studies also name the Srisailam Formation as the top of the Nallamalai Group (eg. Chaudhuri *et al.* 2002; Saha 2002), however for the purposes of this study the Nallamalai Group will only refer to the Bairenkonda and Cumbum Formations. The base of the Bairenkonda Formation consists of coarse to pebbly sandstones that are overlain by a hummocky cross stratified sandstone of shallow shelf origin (Chaudhuri *et al.* 2002). The transition to the finer grained siltstones, shales and dolomites of the Cumbum Formation is thought to represent a major transgressional event (Chaudhuri

et al. 2002). The presence of ash beds, mass-flow conglomerates and slumped beds suggest syn-sedimentary faulting and volcanism during the deposition of the Cumbum Formation (Chatterjee & Bhattacharji 2001; Chaudhuri *et al.* 2002).

Current age constraints of the Nallamalai Group have placed maximum depositional ages of 1660 ± 21 Ma on the Bairenkonda Formation and 913 ± 11 Ma on the younger Cumbum Formation, however this age was produced from a single zircon grain and must be treated with caution as contamination cannot be ruled out (Mackintosh 2010). The ~1575 Ma (Rb-Sr model age, Crawford & Compston 1973) Vellaturu Granite in the eastern boundary of the NFB has been used as a minimum depositional age for the Nallamalai Group rocks. A more definite age of 1350 ± 52 Ma is provided by cross-cutting kimberlites that are found cutting the Bairenkonda Formation in the centre of the belt.

Saha (2002) suggests three phases of deformation, D_1, D_2 and D_3, within the Nallamalai Group. D_1 structures are represented by tight to isoclinal folds and D_2 structures are represented by NE trending tight to open folds with variable plunge, indicating the control of large domal structures. Due to the presence of similar deformation with in xenoliths of Nallamalai rocks in the ~1575 Ma Vellaturu Granite, these deformation events are thought to be associated with the deformation of the EGB at ~1600 Ma (Saha 2002). D_3 structures are represented by E-W trending folds and cleavage. This deformation event is thought to have also affected the much younger Kurnool Group, whose age is poorly constrained but is thought to have been deposited after ~1090 Ma (Dobmeier & Raith 2003). With this constraint in mind, it is likely that D_3 structures are related to either the ~1000 Ma amalgamation of Rodinia or the ~550 Ma amalgamation of Gondwana.

3.0 FIELD WORK AND STRUCTURAL INTERPRETATION

3.1 Field work and image interpretation

Due to the large study area, limited accessibility and time constraints, a detailed structural map could not be produced in the field. Instead, structural interpretation of optimally processed 15 m resolution panchromatic Landsat 7 ETM images was accompanied by reconnaissance mapping in the field. Interpretation was aided by the use of a reprocessed 90 m resolution SRTM digital elevation model (DEM) along with three-dimensional Google Earth satellite images. Figure 4 visually outlines the process undertaken to interpret geological features from these images using topography-bedding relationships and discontinuity theories to infer dip and dip direction of beds, axial traces of folds, and fault orientation. Interpreted features along with measured field data were overlain on to the Landsat ETM image using the spatial analysis and mapping program ArcGIS. An interpreted structural sketch of the study area is produced in Figure 5.

Whilst conducting field work, it was noted that there is very little discernible difference between what is currently differentiated as the Bairenkonda and Cumbum Formations. Whilst there is a distinguishable difference between the homogenous quartzite beds of the Bairenkonda Formation and the interlayered sandstones and shales of the Cumbum Formation, there was no evidence of any form of unconformable contact between the two. This made it hard to place precise lithological boundaries on the map and thus, for the purpose of this study, the Nallamalai Group was treated as a single, continuous lithology.

3.2 Cross sections

Twenty five meter interval topographic contours of the study area were computed and imported into the advanced structural modelling software MOVE 2D. Cross

sections were originally drawn by hand before being scanned and imported into MOVE 2D. Measured and interpreted data were then projected onto the sketch.

Two geological sketches have been constructed perpendicular to the main N-S trending structures of the NFB from the Cuddapah Basin to the west, through the fold belt, and into the NSB to the east. The two section lines are shown in Figure 6a and Figure 7a. Figure 6b shows a geological sketch across the entire Cuddapah Basin and into the NSB. This details the constraints of the relationships between sub-basins. Section I is shown in Figure 6c and Section II is shown in Figure 7b. Due to the arcuate nature of the fold belt, Section I is a W-E traverse through the N-S trending structures of the NFB, whilst Section II is a NW-SE traverse through the SW-NE trending structures. Section I starts in the Kurnool Subgroup near the town of Nandyal and ends in the NSB east of the town of Giddalur. The contact between the Kurnool Group and the Nallamalai Group was interpreted as a large east dipping thrust fault. This is due to the strong N-S linear feature on the DEM that correlates with the contact between the Kurnool Group and Nallamalai Group sediments.

The structural geometry of Section I is characterised by east dipping thrust stacks. Two of the interpreted fault blocks contain large scale folding. The west most set of folds are slightly asymmetric with steeper western limbs and shallower eastern limbs suggesting vergence towards the east. The east most set of folds are upright isoclinal folds. All other fault blocks present continuous eastward dipping bedding. Bedding measurements show much steeper dips directly east of each thrust fault before shallowing out significantly towards the west. A sudden transition from shallow dipping beds in the footwall of a thrust fault to steeply dipping beds in the hanging wall was subsequently used to interpret thrust faults where they were not immediately apparent by visual interpretation.

Section II begins in the Srisailam sub-basin, near the town of Srisailam, and ends in the NSB, near the town of Konakanametla. The contact between the Srisailam Formation and Nallamalai Group is largely undefined and has been described as both an unconformity and a thrust contact (eg. Dasgupta & Biswas 2006; Saha & Tripathy 2011, In Review). The contact between the two represents the transition between the largely undeformed Srisailam Formation and the heavily folded Nallamalai Group. Fieldwork along this section did not reveal any distinct difference between the upper Srisailam Formation and the Nallamalai Group and the possibility of the two being lateral equivalents cannot be ruled out.

This section cuts through a major domal structural named the Iswarakuppam Dome. The domal structure of the bedding shows radial dips around the edges of the dome, whilst the centre appears to be relatively flat lying. The dome exposes mainly Nallamalai rocks and shows no sign of basal Cuddapah succession. Because of this, the mechanism of formation of the dome is controversial. Dasgupta and Biswas (2006) suggest that doming was probably due to the uprising of granitic magma. This is supported by the presence of other large domes with granitic cores that have intruded into the north-eastern corner of the basin. To the east of the Iswarakuppam dome, alluvial cover makes it hard to visually interpret the underlying structure; however a small number of field measurements suggest the beds are consistently dipping towards the east, possibly suggesting a series of east dipping faults similar to those in Section I.

4.0 ANALYTICAL METHODS

4.1 U-Pb Detrital Zircon Geochronology

4.1.1 SAMPLE PREPARATION

Samples were collected during three weeks of field work based in the NFB and surrounding areas. Samples were chosen based on their location, mineralogy, and perceived potential for containing heavy minerals such as zircon. Whole rock samples were cut using a diamond saw and crushed using a standard jaw crusher. Crushed sample was then milled using a tungsten carbide vibrating mill, and sieved through 425µm and 75µm mesh. Sample that was between 75µm and 425µm was taken for mineral separation.

Mineral separation involved hand panning and methylene iodide heavy liquid separation. Zircon grains were hand-picked from the heavy mineral separate. Where possible, approximately 200-300 zircon grains per sample were mounted in epoxy resin discs, before being polished to expose internal textures of the zircon grains.

Zircon mounts were imaged at Adelaide Microscopy using a Phillips XL20 scanning electron microscope (SEM), with a Gatan cathodoluminescence (CL) detector. Backscattered electron (BSE) and CL images were obtained for each sample to check grains were in fact zircon, and to detail zonation within individual grains.

4.1.2 LA-ICPMS OPERATING PROCEDURES AND DATA REDUCTION

Laser Ablation – Inductively Coupled Plasma Mass Spectrometry (LA-ICPMS) U-Pb analysis was conducted at Adelaide Microscopy using a New Wave 213nm Nd-YAG laser coupled with an Agilent 7500cs ICPMS. Zircon grains were ablated in a helium atmosphere using a repetition rate of 5 Hz, a beam diameter of 30µm and an

intensity of 75-80% (~6-8 J/cm^2). Data acquisition involved 25 seconds of background measurement, 5 seconds of beam stabilisation and 70 seconds of sample ablation.

Ablation and machine fractionation corrections were made using the standard GEMOC GJ-1 (TIMS normalisation data: $^{207}Pb/^{206}Pb$ = 608.3 Ma, $^{206}Pb/^{238}U$ = 600.7 Ma and $^{207}Pb/^{235}U$ = 602.2 Ma (Jackson *et al.* 2004)), and checked using an internal standard Plesovice ($^{207}Pb/^{206}Pb$ = 339 Ma, $^{206}Pb/^{238}U$ = 337.13 (Slama *et al.* 2008)). GJ-1 gave a mean $^{206}Pb/^{238}U$ age of 600.7 ± 1.1 Ma (MSWD 0.49), whilst Plesovice gave a mean $^{206}Pb/^{238}U$ age of 340 ± 3.1 Ma (MSWD of 2.8). Analyses that produced a Pb^{204} count of 100 cps or greater were discarded.

Age calculations were conducted using the software program GLITTER (Griffin *et al.* 2008). Where not specified, analyses younger than 1000 Ma are quoted as the $^{206}Pb/^{238}U$ age, whilst analyses older than 1000 Ma are quoted as the $^{207}Pb/^{206}Pb$ age. This is due to the reduced precision of $^{207}Pb/^{206}Pb$ ages for analyses younger than 1000 Ma (Ireland *et al.* 1998; Collins *et al.* 2007).

4.2 Hf Isotope Analysis

The Hf isotope analyses reported here were carried out in-situ using the LA-MC-ICPMS at Waite (CSIRO) Campus, South Australia. Samples analysed were the same ones used for U-Pb geochronology and therefore sample preparation is outlined in section 3.1. Only concordant grains (90-110%) were analysed with Hf analysis in the same CL domain as targeted in U-Pb LA-ICPMS geochronology. Zircon grains were ablated with a New Wave UP-193 Excimer laser (193nm) using a 4ns pulse length, 5 Hz repetition rate, 50 µm spot size, and irradiance of ~10 J/cm^2. The ablated material travelled through a He ablation atmosphere mixed with Ar gas.

Measurements were made using a Thermo-Scientific Neptune Multi Collector ICP-MS equipped with Faraday detectors and $10^{12}\Omega$ amplifiers. Analyses used a dynamic measurement routine with: Ten 0.524 second integrations on ^{171}Yb, ^{173}Yb, ^{175}Lu, ^{176}Hf(+Lu+Yb), ^{177}Hf, ^{178}Hf, ^{179}Hf and ^{180}Hf; one 0.524 second integration on ^{160}Gd, ^{163}Dy, ^{164}Dy, ^{165}Ho, ^{166}Er, ^{167}Er, ^{168}Er, ^{170}Yb and ^{171}Yb, and, one 0.524 second integration of Hf oxides with masses ranging from 187 to 196 amu. An idle time of 1.5 seconds was included between each mass change to allow for magnet settling and to negate any potential effects of signal decay. This measurement cycle is repeated 15 times to provide a total maximum measurement time of 3.75 minutes including an off-peak baseline measurement. This dynamic measurement routine is used to allow for the monitoring of oxide formation rates and REE content of zircon and provide the option to correct for REE-oxide interferences as necessary. Hf oxide formation rates for all analytical sessions in this study were in the range 0.1-0.07%.

Hf mass bias was corrected using an exponential fractionation law with a stable ^{179}Hf/^{177}Hf ratio of 0.7325. Yb and Lu isobaric interferences on ^{176}Hf were corrected for following the methods of Woodhead et al. (2004). ^{176}Yb interference on ^{176}Hf was corrected for by direct measurement of Yb fractionation using measured ^{171}Yb/^{173}Yb with the Yb isotopic values of Segal et al. (2003). The applicability of these values were verified by analysing JMC 475 Hf solutions doped with varying levels of Yb with interferences up to ^{176}Yb/^{177}Hf= ~0.5. Lu isobaric interference on ^{176}Hf corrected using a ^{176}Lu/^{175}Lu ratio of 0.02655 (Vervoort *et al.* 2004) assuming the same mass bias behaviour of as Yb. Set-up of the system prior to ablation sessions was conducted using analysis of JMC475 Hf solution and an AMES Hf solution. Confirmation of accuracy of the technique for zircon analysis was monitored using a combination of the Plesovice, Mudtank and QGNG standards. The average value for Plesovice for the analytical session was 0.282479 (2SD=0.000012, n=17). This

compares to the published value of 0.282482 ± 0.000013 (2SD) by Slama et al. (2008).

T_{DM} and $T_{DM\ crustal}$ were calculated using ^{176}Lu decay constant after Scherer et al., (2001). $T_{DM\ crustal}$ was calculated using the methods of Griffin et al. (2002) with an average crustal composition of $^{176}Lu/^{177}Hf=0.015$.

4.3 LA-ICPMS Trace Element Zircon Analysis

Trace element analysis was performed on samples EA01 and EA08 following U-Pb geochronology analysis (sample preparation outlined in section 3.1). Zircon grains were only analysed if they were within 10% concordance (90-110%), and were analysed within the same CL domain as the U-Pb analysis. After U-Pb analysis, zircon grains were analysed using the Cameca SX51 microprobe at Adelaide Microscopy. The microprobe was used with an accelerating voltage of 15 kV and a beam current of 20 nA. This analysis provided a precise Hf oxide percent measurement to be used as an internal standard on the LA-ICPMS. Laser ablation was conducted using a 55 µm spot size at 75% intensity (~10 J/cm^2) and 5 Hz repetition rate. Acquisition time was divided into 40 seconds of background measurement, 10 seconds of beam stabilisation and 50 seconds of laser ablation. External standard NIST610 was used to correct for fractionation and mass bias (Pearce *et al.* 1997). Analyses were internally corrected using the Hf values acquired previously. Data was corrected using the software program GLITTER (Griffin *et al.* 2008).

4.3.1 REE CHEMISTRY

Chondrite normalised trace element values have been plotted on a chondrite normalised spider diagram where normalised concentration is plotted on a

logarithmic scale against multiple elements. This produces a REE 'pattern' which can then be used to compare against known REE patterns for specific rock types as well as the identification of anomalies. Anomalous values of Ce and Eu are a feature of igneous zircon grains. These anomalies are quantified by comparing the measured concentration of Eu or Ce with an expected concentration obtained by interpolating between the normalised values of the elements that sit either side of it (Eu* or Ce*). These anomalies are calculated using Eu/Eu* = $\frac{Eu_N}{\sqrt{(La_N\ X\ Pr_N)}}$ for the Eu anomaly and Ce/Ce* = $\frac{Ce_N}{\sqrt{(Sm_N\ X\ Gd_N)}}$ for the Ce anomaly.

4.3.2 TI-IN-ZIRCON THERMOMETRY

This study has employed the use of the Ti in zircon thermometer of Watson et al. (2006) and subsequent revisions of Ferry & Watson (2007). The application of this thermometer provides an estimate of the closure temperature of the zircon analysed. This can be used as an indication of the source rock, thus providing another dimension in the identification of sediment provenance.

The Ti in zircon thermometer is based on the limited and temperature dependent exchangeability of Ti within zircon. It is calibrated using the combined results of trace element analysis on natural and synthetic examples of zircon who crystallisation conditions are independently constrained. The log-linear relationship between Ti (ppm) and reciprocal absolute temperature (K) is presented below:

$$\log(Ti_{zircon}) = \frac{(5.711 \pm 0.072) - (4800 \pm 86)}{\mathrm{T(K)} - \log(\partial_{SiO_2}) + \log(\partial_{TiO_2})} \qquad (1)$$

Due to the uncertainty of ∂_{SiO_2} and ∂_{TiO_2}, values of 1 and 0.6 have been applied respectively as of Ferry and Watson (2007). Although the use of these assumed

values may produce temperatures outside the error range of actual temperatures calculated if ∂_{SiO_2} and ∂_{TiO_2} were known, the accuracy of using assumed activity values is much greater than if activities are disregarded all together.

5.0 ANALYTICAL RESULTS

A summary table of all analytical results for all samples is presented in Table 1.

5.1 U-Pb Detrital Zircon Geochronology

U-Pb zircon geochronological analysis was conducted on seven samples collected from different locations within the Nallamalai Group (Figure 3). This was conducted primarily to constrain the maximum depositional age of the formation. It also presents a spectrum of ages within each sample, which provides valuable information on the source of sediments.

U-Pb zircon data is presented in Appendix 1. Probability density diagrams for each sample separately (Figure 8a-g), as well as the Nallamalai group as a whole (Figure 8h) have been presented. Concordia diagrams for each sample are presented in Figure 9 and Figure 10 with insets of a representative CL image of each sample. CL information is presented in Table 2 for each of the samples described below.

5.1.1 SAMPLE EA01

This sample is a medium to fine grained clean quartzite containing very fine dark mineral banding. It was taken from the eastern border of the Nallamalai Group at GPS location 16˚05’41.1”N, 79˚41’40.6”E (Figure 3), very close to the contact between the Nallamalai Group and the NSB. A representative sample set of 108 zircon grains were ablated. Of this, 63 zircon grains were between 90 and 110 percent concordant (Figure 9), with 2 analyses discounted due to high counts of common lead (Pb^{204}). The main population of zircon grains occurs at 2525 ± 11 Ma

(number of zircon grains, n=46) (Figure 8a). Smaller peaks occur at 2345 ± 20 Ma (n=5) and 2935 ± 27 (n=2). The youngest population of zircon grains gives a mean weighted average of 2158 ± 30 Ma (n=2). The youngest 90-110% concordant analysis (spot073) yielded a $^{207}Pb/^{206}Pb$ age of 1882 ± 22 Ma.

5.1.2 SAMPLE EA04

This sample is a muscovite rich, arenaceous schist. It was taken from the eastern border of the Nallamalai Group at GPS location 15˚34'41.9"N, 79˚18'06.4"E (Figure 3), very close to the contact between the Nallamalai Group and the NSB. This sample was taken from a shaley layer that was interbedded with a clean quartz arenite. A representative sample set of 90 zircon grains were ablated. Of this, 68 were between 90 and 110 percent concordant (Figure 9), with 4 analyses discounted due to high counts of common lead (Pb^{204}). The main population of zircon grains occurs at 2489 ± 19 Ma (n=24) (Figure 8). Secondary peaks occur at 2031 ± 22 Ma (n=11) and 1875 ± 25 Ma (n=10). Much smaller peaks also occur at 2757 Ma (n=4) and 3316 (n=2). The youngest population of zircon grains gives a mean weighted average of 1862 ± 17 Ma (n=9). The youngest 90-110% concordant analysis (spot09) yielded a $^{207}Pb/^{206}Pb$ age of 1683 ± 25 Ma.

5.1.3 SAMPLE EA05

This sample is a ferruginous, massive sandstone. It was taken from the central area of the NFB at GPS location 15˚25'37.5"N, 78˚45'42.1"E (Figure 3), It was taken from shallowly dipping beds close to a contact with steeply dipping shaley beds that were thrust over the top of these sandstone beds. A representative sample set of 85 zircon grains were ablated. Of this, 48 were between 90 and 110 percent concordant (Figure 9).The main population of zircon grains occurs at 2499 ± 18 Ma (n=17) (Figure 8). Three secondary peaks occur at 1910 Ma (n=5), 1844 Ma (n=5) and 1767 Ma (n=6). Smaller peaks occur at 2715 Ma (n=4), 2360 Ma (n=4) and 2007 Ma (n=2).

The youngest population of zircon grains gives a mean weighted average of 1767 ± 17 Ma (n=6). The youngest 90-110% concordant analysis (spot20) yielded a $^{207}Pb/^{206}Pb$ age of 1661 ± 20 Ma.

5.1.4 SAMPLE EA06

This sample is a fine grained, clean quartzite with thick heterogeneous dark banding. It was taken from the western border of the Nallamalai Group at GPS location 15˚11'12.0"N, 78˚38'01.8"E (Figure 3). This sample was very zircon poor with only 17 zircon grains able to be extracted. Of this, 9 were between 90 and 110 percent concordant (Figure 9). The main population of zircon grains occurs at 2515 Ma (n=3) (Figure 8), with secondary peaks at 2604 Ma (n=3) and 2465 Ma (n=2). The youngest population of zircon grains gives a mean weighted average of 2465 ± 26 Ma (n=3). The youngest 90-110% concordant analysis (spot14) yielded a $^{207}Pb/^{206}Pb$ age of 1843 ± 32 Ma.

5.1.5 SAMPLE EA07

This sample is a highly deformed, medium grained sandstone that was interbedded with siltstones and shales. It was taken from the Tippayapalem Reservoir at GPS location 15˚41'25.0"N, 79˚09'59.8"E (Figure 3). A representative sample set of 80 zircon grains were ablated. Of this, 65 were between 90 and 110 percent concordant (Figure 10), with 2 analyses discounted due to high counts of common lead (Pb^{204}). The main population of zircon grains occurs at 2470 Ma (n=25) (Figure 8), with secondary peaks at 2666 Ma (n=10) and 1850 Ma (n=10). A series of smaller, but significant peaks occur between 1913 Ma and 2340 Ma with a total number of 18 zircon grains between these ages. The youngest population of zircon grains gives a mean weighted average of 1851 ± 18 Ma (n=9). The youngest 90-110% concordant analysis (spot28) yielded a $^{207}Pb/^{206}Pb$ age of 1783 ± 71 Ma.

5.1.6 SAMPLE EA08

This sample is a medium grained quartzite with well defined, thin, dark mineral banding. It was collected at GPS location 15˚45'43.5"N, 79˚12'29.2"E (Figure 3). A representative sample set of 80 zircon grains were analysed. Of this, 71 were between 90 and 110 percent concordant (Figure 10). The main population of zircon grains occurs at 2515 Ma (n=31) (Figure 8), with secondary peaks occurring at 2689 Ma (n=9), 2310 Ma (n=5), 2200 Ma (n=5) and 1890 Ma (n=13). The youngest population of zircon grains give a mean weighted average of 1867 ± 15 (n=7). The youngest 90-110% concordant analysis (spot21) yielded a $^{207}Pb/^{206}Pb$ age of 1836 ± 20 Ma.

5.1.7 SAMPLE CU10-09

This sample is a laminated quartz arenite. It was collected at GPS location 15˚23'34.2"N, 78˚39'48.3"E (Figure 3). A representative collection of 96 zircon grains were ablated. Of this, 58 were between 90 and 110 percent concordant (Figure 10). The main population of zircon grains occurs at 2538 Ma (n=35) (Figure 8), with secondary peaks at 1850 Ma (n=13), 2098 Ma (n=7), 3074 Ma (n=2), and a single grain at 2842 Ma. The youngest population of zircon grains gives a mean weighted average of 1781 ± 27 Ma (n=3). The youngest 90-110% concordant analysis (spot53) yielded a $^{207}Pb/^{206}Pb$ age of 1774 ± 21 Ma.

5.2 Hf Isotope Analysis

Hf isotope analysis was conducted on five of the samples, EA01, EA04, EA05, EA08 and CU10-09, which were analysed for U-Pb geochronology. Hf analysis, in conjunction with U-Pb geochronology, provides information on the crustal evolution of the zircon being analysed, that is whether it originated from a juvenile or evolved

crustal source. Hf analysis is conducted primarily to provide a secondary source of information, along with geochronology, to constrain the provenance of sediments.

Hf isotope data is reported in Appendix 2. A total of 74 analyses were obtained from 5 samples. Eighteen analyses produced $^{176}Hf/^{177}Hf$ 2 standard errors of >0.00015 and have therefore been discarded. A number of analyses produced $^{176}Hf/^{177}Hf$ 2 standard errors of between 0.0001 and 0.00015, these have been left in the data set but have been coloured grey in Appendix 2 and Figure 10 and Figure 11 to highlight the higher uncertainty of these readings. The data are plotted as ε_{Hf} versus U-Pb age in Figure 10. An initial $^{176}Hf/^{177}Hf$ vs U-Pb age plot is presented in Figure 11 using a bulk crust $^{176}Hf/^{177}Hf$ ratio of 0.015. There is no discernible difference in results evident between samples. Therefore, to give context to the results, they have been summarised below by grouping $^{207}Pb/^{206}Pb$ ages in terms of detrital peaks (Figure 8h) instead of by sample.

A total of 14 grains that returned $^{207}Pb/^{206}Pb$ ages between 1925 Ma and 1750 Ma were analysed. They produced initial $^{176}Hf/^{177}Hf$ values ranging between 0.280943 and 0.281622 and ε_{Hf} values ranging between -23.37 and 0.71. Corresponding $T_{DM(crustal)}$ ages ranged between 3.89 and 2.45 Ga.

A total of 14 grains that returned $^{207}Pb/^{206}Pb$ ages between 2540 Ma and 1980 Ma were analysed. They produced initial $^{176}Hf/^{177}Hf$ values ranging between 0.28101 and 0.281507 and ε_{Hf} values ranging between -13.03 and 2.58. Corresponding $T_{DM(crustal)}$ ages ranged between 3.51 and 2.54 Ga.

A total of 23 grains that returned $^{207}Pb/^{206}Pb$ ages between 2650 Ma and 2451 Ma were analysed. They produced initial $^{176}Hf/^{177}Hf$ values ranging between 0.280776

and 0.281406 and ε_{Hf} values ranging between -14.55 and 10.97. Corresponding $T_{DM(crustal)}$ ages ranged between 3.85 and 2.44 Ga.

A total of 5 grains that returned $^{207}Pb/^{206}Pb$ ages between 2970 Ma and 2680 Ma were analysed. They produced initial $^{176}Hf/^{177}Hf$ values ranging between 0.280747 and 0.281246 and ε_{Hf} values ranging between -7.84 and 6.38. Corresponding $T_{DM(crustal)}$ ages ranged between 3.71 and 2.75 Ga.

5.3 Trace Element Zircon Analysis

Trace element data were collected from zircon samples that had already been analysed for U-Pb geochronology. It was conducted primarily for the purpose of titanium (Ti) thermometry and rare earth element (REE) chemistry. The main applications for measuring trace element abundances in zircon for this study are: 1) Using REE composition as an indicator of source rock type as of Belousova et al. (2002) and 2) Using Ti-in-zircon thermometry to estimate the temperature at which the zircon formed at using the methods of Watson et al. (2006). The use of these two tools in conjunction with U-Pb geochronology can aid in the constraint of sediment provenance.

Following the methods of Belousova et al. (2002), scatter plots have been produced for Y vs U, Ce/Ce* vs Eu/Eu*, Y vs Yb/Sm and Y vs Ce/Ce*. These plots have been overlain the plots produced from Belousova et al. (2002) and are shown in Figure 13.

5.3.1 SAMPLE EA01

Seventeen concordant zircon grains underwent trace element analysis. Chondrite normalised REE analysis data is presented in Table 3, and a spider diagram is presented in Figure 14. ΣREE range from 674 - 2979 ppm with an average of 1575

ppm. The chondrite normalised REE patterns for these zircon grains are characterised by generally steep LREE patterns with the exception of a few analyses that are relatively enriched in LREE (Sm_N/La_N = 0.78 – 26.11, Ave = 7.68). All analyses are enriched in HREE (Lu_N/Sm_N = 7.02 – 102.1, Ave = 39.48), and show a positive Ce anomaly (Ce/Ce* = 1.15 – 42.46, Ave = 6.34) and a negative Eu anomaly (Eu/Eu* = 0.26 – 0.94, Ave = 0.54).

Using the Ti-in-zircon thermometer this sample produced temperatures between 748±76 ˚C and 988±39 ˚C with a mean weighted average of 872 ± 30 ˚C. A full list of temperatures calculated for the sample is presented in Table 4

5.3.2 SAMPLE EA08

Eighteen concordant zircon grains underwent trace element analysis. 1 analysis was discarded due to the presence of an inclusion within the zircon grain. chondrite normalised REE analysis data is presented in Table 5, and a spider diagram is presented in Figure 15. ΣREE range from 496 - 3663 ppm with an average of 1917 ppm. The chondrite normalised REE patterns for these zircon grains are characterised by generally steep LREE patterns with the exception of a few analyses that are relatively enriched in LREE (Sm_N/La_N = 1.18 – 194.9, Ave = 25.05). All analyses are enriched in HREE (Lu_N/Sm_N = 5.56 – 111.89, Ave = 34.99), and show a positive Ce anomaly (Ce/Ce* = 1.04 – 48.4, Ave = 9.01) and a general negative Eu anomaly (Eu/Eu* = 0.19 – 0.91, Ave = 0.66), with the exception of one analysis (ree29) that produced a positive Eu anomaly (Eu/Eu* = 1.36).

Temperatures calculated for this sample ranged between 752 ± 72 ˚C and 1015 ± 42 ˚C with a mean weighted average of 903 ± 36 ˚C. A full list of temperatures calculated for the sample is presented in Table 6

6.0 DISCUSSION

6.1 Age constraints of the Nallamalai Group

Mackintosh (2010) has previously constrained the maximum depositional age of the Nallamalai Group to 913 ± 11 Ma. This age was inferred from a single grain, one of only seven concordant analyses conducted on a sample taken from the Cumbum Formation which sits stratigraphically at the top of the Nallamalai Group. This sample contained no other grains of similar age to this and the youngest population within this sample produced a mean weighted average of 1753 ± 60 Ma.

In contrast, this study which analysed 382 concordant zircon grains from the Nallamalai Group produces a youngest concordant analysis of 1661 ± 20 Ma. This analysis, along with a second grain of similar age, produces a mean weighted average of 1669 ± 31 Ma. This is supported by the findings of Mackintosh (2010) who gives a $^{207}Pb/^{206}Pb$ maximum depositional age of 1660±22 Ma, from one single grain, for the lower Nallamalai Group (Bairenkonda Formation). As these ages overlap within error, this provides evidence for a *ca* 1660 Ma population. The results from this, more comprehensive, U-Pb detrital zircon study suggests that the 913 Ma grain analysed by Mackintosh (2010) is suspect, and may represent contamination.

A minimum age of deposition for the Nallamalai Group is given by the Vellaturu Granite which is in contact with the Nallamalai Group and contains xenoliths of deformed Nallamalai Group rocks (Saha 2002). The Rb-Sr model age for the intrusive Vellaturu Granite is 1575 ± 20 Ma (Crawford & Compston 1973). A further constraint is provided by an $^{40}Ar/^{39}Ar$ age determined for the Chelima Lamproite that is quoted as ~1400 Ma (Chalapathi Rao *et al.* 1999). Therefore this study proposes that the deposition of the Nallamalai Group occurred between 1661 ± 20 and 1575 ± 20 Ma.

6.2 Provenance of the Nallamalai Group sediments

The sediments of the Nallamalai Group have not undergone any tectonothermal event that would create or alter the zircon grains deposited in the sediments. Consequently, ages obtained during U-Pb geochronology can be related to tectonothermal events that have occurred in source regions. Sediments of the Nallamalai Group show a dominant detrital zircon age peak at ~2500 Ma, a secondary peak at ~1850 Ma, a range of Paleoproterozoic ages between these peaks, and a small peak at ~2700 Ma (Figure 8h). This study will firstly consider source regions that conform to these age requirements.

It is also important to use methods such as Hf isotope analysis in conjunction with U-Pb geochronology when tracing the provenance of sediments (Howard *et al.* 2009). The general lack of available Hf isotope data limits its usefulness in acting as a provenance tracing tool. However, given that Lu-Hf and Sm-Nd isotope systems behave in a very similar manner during most magmatic processes, it is possible to compare Hf and Nd isotopic compositions. Vervoort et al. (1999) has shown that a single coherent trend ($\varepsilon_{Hf} = 1.36\varepsilon_{Nd} + 2.95$) exists for a terrestrial array of samples. This makes it possible to compare ε_{Nd} values from previous studies with the ε_{Hf} values produced in this study, helping to identify or rule out possible source regions.

The large range of U-Pb zircon ages suggests that the sediments of the Nallamalai Group are either sourced from several different source regions, or a single source region composed of rocks of different ages, or a combination thereof. Hf isotope results suggest juvenile input at ~2500 Ma with younger grains becoming much more evolved (Figure 11). The isotopic evolutionary trend line fitted to Figure 12 shows that the younger grains have similar isotopic evolutions to the 2500 Ma zircon grains.

The dominant detrital peak at ~2500 Ma suggests that a dominant portion of sediments were sourced from the adjacent East Dharwar Craton which is dominated by 2600-2500 Ma granitic intrusions (Jayananda *et al.* 2000). The smaller peak at ~2700 Ma as well as the few single grains aged between 2900 Ma and 3400 Ma can be accounted for by derivation from the Sargur Group (3.1-3.3 Ga) and Dharwar Supergroup (2.6-2.9 Ga) in the West Dharwar Craton (Jayananda *et al.* 2008).

Zircon grains with a U-Pb ages of ~2500 Ma show a large range of ε_{Hf} values (-15 to +11) suggesting that there is a mixture of juvenile and evolved material that correspond to a $T_{DM\ (crustal)}$ between 3.85 and 2.44 Ga. Most zircon grains with U-Pb ages of < 2500 Ma produced negative ε_{Hf} values (-23 to 0) with only four analyses producing very low positive values (0 to 3). Jayananda et al. (2000) reports ε_{Nd} values between -8 and +3 for the ~2500 Ma Dharwar Craton intrusions, which translates to a an ε_{Hf} range of -8 to +7. This correlates well with ε_{Hf} data presented from the Nallamalai Group and allows the Dharwar Craton to be a source component.

Whilst the detrital zircon peaks that lie between 2400 Ma and 1900 Ma are small, they are still significant. The main peaks occur at ~2300 Ma, ~2200 Ma and ~2050 Ma, with a range of individual zircon ages in between. Widespread Paleoproterozoic dyking events in the Dharwar Craton have been precisely dated using U-Pb dating techniques by French and Heaman (2010). These dykes have been dated at between 2181-2177 Ma, 2221-2209 Ma and 2369-2365 Ma, which suggests it is a possible source region for the range of Paleoproterozoic ages seen in the Nallamalai Group sediments. However, U-Pb dating of sediments from the Ongole Domain in

the EGB has also produced a similar range of detrital zircon ages with peaks at ~2150 Ma, ~2300 Ma and ~2400 Ma (Henderson 2011), which may suggest an additional or alternative source region.

Previous work by Mackintosh (2010) has suggested that the presence of a detrital zircon peak at ~1800 Ma within the Nallamalai Group may suggest sediment was being sourced from the NSB which experienced a period of felsic magmatism that has been dated at 1868 ± 6 Ma and 1771 ± 8 Ma (Vasudevan *et al.* 2003). However, very recent U-Pb geochronology by (Henderson 2011) has found detrital zircon grains aged between 1810 Ma and 1900 Ma in the Ongole Domain. This suggests the Ongole Domain may be an additional or alternative source region for the ~1800 Ma sediments in the Nallamalai Group. Another possible source of 1800-1900 Ma detrital zircon grains is the mafic-ultramafic sill complex that was emplaced within the Tadpatri Formation at ~1900 Ma (Anand *et al.* 2003).

Anand et al. (2003) reports ε_{Nd} values for the ~1900-1800 Ma mafic-ultramafic sills in the Tadpatri Formation of -10 to +1 which translates to ε_{Hf} of -11 to +4. This is comparable to the ε_{Hf} range of -23 and +1 produced for zircons of this age range from the Nallamalai Group. A very limited Hf isotope data set for the Ongole Domain quotes an ε_{Hf} range of -9 to -2 for zircon grains with a U-Pb age of between 1900 and 1800 Ma (Henderson 2011). This is similar to the ε_{Hf} values of the Nallamalai Group, especially as the majority of data from the Nallamalai Group lie between -9 and -2.

The small detrital peak at ~1660 Ma that represents the maximum depositional age of the Nallamalai Group is produced by zircon grains that appear to be of a metamorphic nature when examined under CL imaging. This compares with a

metamorphic event in the Ongole Domain that has been dated between 1590 Ma and 1690 Ma with a mean age of ~1640 Ma (Henderson 2011), supporting the southern Eastern Ghats as a possible source region.

Data collected from trace element zircon analysis can be compared to a recent study by Belousova et al. (2002) that attempts to correlate trace element composition with a source rock type for igneous zircons. Although not all of the zircons in this study are igneous, the majority of analysed zircons display igneous characteristics, and these were targeted for analysis. Whilst very few REE patterns from the Nallamalai Group show a strong correlation with a single source rock pattern, most of the data is comparable to the REE pattern of an average granitoid (Figure 14 and Figure 15). Ce anomalies (represented by Ce/Ce*) of a typical granitoid are between 1 and 10, however are mostly restricted to a range of 1 to 3. The zircons analysed in this study produced Ce anomalies that averaged 9 and 6, however the majority of values were between 1 and 3 with a few large outliers causing larger averages.

Further evidence for a granitic source is shown in Figure 13 where REE data from the Nallamalai Group is overlain on the fields of zircon composition produced by Belousova et al. (2002). In all four plots, the majority of data lies within the granitoid field and more specifically in the granodiorite and tonalite field. The crystallisation temperatures of zircons analysed from the Nallamalai Group are summarised in Table 4 and Table 6. These are similar to the crystallisation temperature of granite (between 800 and 900 ˚C). This supports an original granitic source for the majority of zircon grains analysed.

6.3 Structural evolution of the NFB

The structural features of the NFB have been outlined in previous studies (Saha 2002; Mukherjee 2003; Saha & Chakraborty 2003).This is the first study to construct

a cross section through the Cuddapah Basin and into the NSB. The recent maximum depositional ages placed on the Gandikota Formation (~1207 Ma, Falster 2011) and the Nallamalai Group (~1660 Ma, this study) confirm the contact between the Nallamalai Group and the Kurnool Group as an east dipping thrust fault. This is also evidenced by a strong N-S trending linear feature on the DEM image.

The abundance of east dipping thrust faults suggests a crustal scale detachment fault at the base of the Nallamalai Group. Whilst large amounts of crustal shortening make it hard to infer the thickness of the Nallamalai Group sediments, the short wavelength of the westward verging folds shown in Figure 6c suggests the deformed sediments would not exceed ~2-3 km in depth. This inference is the basis for the placement of a detachment fault propagating off the large scale thrust fault that brings the NSB into contact with the NFB.

The contact between the Nallamalai Group and the Srisailam Formation remains largely undefined in this study. Fieldwork in the area revealed little discernable difference between the upper Nallamalai Group and the Srisailam Formation and no visible contact between the two was observed. It has been represented by an unconformity in Section II largely due to the works of previous studies (eg. Sinha *et al.* 1995; Dasgupta & Biswas 2006). Current work by Saha and Tripathy (2011, In Review) states that in some areas, the contact is represented by an east dipping thrust fault that brings the rocks of the Nallamalai Group on top of the Srisailam Formation.

Recent U-Pb detrital zircon geochronology of the Srisailam Formation by Gore (2011) yields inconclusive age constraints, providing a maximum deposition age of ~1787 Ma. The maximum depositional age of the Srisailam Formation, however, can be further constrained by the maximum depositional age of the Nallamalai Group at

~1661 Ma, as the Srisailam must have been deposited simultaneously or after this time.

Saha (2002) suggests three phases of deformation within the NFB, with D_1 and D_2 structures being preserved in the Vellaturu granite. This infers the formation of these structures occurred before ~1575 Ma. D_2 structures are described as the main N-S trending, west verging folds that are shown in cross section in Figure 6c. Assuming the interpretations of Saha (2002) are correct, these structures must have formed after ~1660 and before ~1575 Ma. In this case it is likely they were the result of ongoing collision between the Ongole Domain and the eastern margin of the EDC that has been dated at *ca* 1640 – 1590 Ma (Henderson 2011).

Age constraints on the thrusting of the Nallamalai Group rocks over the Kurnool Group rocks suggests that major westward thrusting cannot have occurred before ~1200 Ma. This study proposes that deformation of the NFB occurred during the 1640 – 1590 Ma collision of the Ongole Domain with the EDC creating the N-S trending open folds, but that major detachment faulting did not occur until after deposition of the Kurnool Group. As the Krishna Province fails to show any record of a ~1000 – 900 Ma event (Dobmeier *et al.* 2006; Henderson 2011), it is suggested that major faulting within the NFB occurred during the Paleozoic amalgamation of the supercontinent Gondwana.

6.4 Basin evolution

Mishra (2011) suggests that the Cuddapah Basin initiated as a rift basin during the breakup of the supercontinent Columbia at *ca* 1.9 Ga. However, this is unlikely to be the case due to a mafic sill that intrudes the lower five kilometres of the Cuddapah Supergroup that have been dated at ~1885 Ma (French *et al.* 2008), and ~1900 Ma (Anand *et al.* 2003). Previous studies by Chatterjee and Bhattacharji (2001) along

with a present study by (Falster 2011) suggest that alluvial fan deposits along with east-trending paleoflow within the Gulcheru Quartzite (Papaghani Group) indicate an extensional setting for the initiation of the Cuddapah Basin between 2400 and 2100 Ma.

The carbonate horizons of the Tadpatri Formation suggest that the Chitravati Group was deposited in a passive margin setting undergoing moderate extension (Falster 2011). This extension is characterised by extensive mafic-ultramafic magmatism within the Cuddapah Basin and nearby Bastar Craton that has been dated at ~1900 Ma (Anand *et al.* 2003; French *et al.* 2008).

This study suggests that the passive margin setting of the Cuddapah Basin evolved into a convergent margin sometime after 1900 Ma, before the collision between the Cuddapah Basin and the Krishna Province at ~1640 Ma (Henderson 2011). This collision caused the uplift of the southern EGB creating crustal flexure directly to the west of the mountain belt; corresponding with the eastern margin of the Cuddapah Basin. A subsequent shift in the depocentre of the Cuddapah Basin towards the east consequently initiated the foreland basin style deposition of the Nallamalai Group sediments.

The Bairenkonda quartzite at the base of the Nallamalai Group suggests a shallow water depositional environment, with paleocurrent data indicating an intertidal environment (Mackintosh 2010). At the onset of a foreland basin, it would be expected that the prominent source of sediments would be largely derived from the foreland (i.e. the Dharwar Craton), however the intertidal depositional environment of the Bairenkonda may explain the mixing of Dharwar Craton and EGB sourced sediments within the Bairenkonda Formation.

As the sediment load increased and crustal thickening in the EGB caused further lithospheric flexure, the Nallamalai sub-basin underwent increased subsidence. This is represented in the Cumbum Formation where sediments show a short transitional sequence from sandstones to shales. The concurrence of younger sediments (~1660-1700 Ma) within rocks of the Cumbum formation may represent a larger detrital input from the EGB, however the prevalence of ~2500 Ma detrital zircons suggests the Dharwar Craton is still a prevailing source of sediment for the Nallamalai Group rocks.

The evolution of the Cuddapah Basin into a foreland basin has largely been suggested due to the overall deepening of the basin to the east. Results of this comprehensive geochronological and isotopic provenance study support this theory; showing significant mixing between sediments derived from both the Dharwar Craton and the southern EGB.

7.0 CONCLUSIONS

This study concludes that there is little discernable difference between the age and source of sediments within the upper (Cumbum) and lower (Bairenkonda) formations of the Nallamalai Group. A robust maximum depositional age of 1661 ± 20 Ma has been placed on the Nallamalai Group. This age, along with a minimum depositional age provided by Crawford and Compston (1973), constrains the timing of deposition of the Nallamalai Group to between 1661 ± 20 Ma to *ca* 1575 Ma. The sediments of the Nallamalai Group were sourced from both the adjacent Dharwar Craton and southern EGB, with the majority of zircons being derived from granitic sources. This mixing of sediments provides further evidence for the Nallamalai sediments being deposited in a foreland basin to the EGB.

The contact between the NFB and the Kurnool group has been confirmed as an east dipping thrust fault. This fault most likely represents a detachment fault that propagates from the large east dipping thrust fault that brings the NSB into contact with the NFB. New age constraints placed on the rocks of the Cuddapah Supergroup suggest that folding occurred within the NFB during the late Paleoproterozoic collision of the southern EGB with the EDC, whilst the major detachment faulting occurred during the early Paleozoic amalgamation of the supercontinent Gondwana.

8.0 ACKNOWLEDGEMENTS

I would like to express a huge thank you to my supervisors Alan Collins and Ros King for all their guidance throughout the year. An extra special thank you goes out to my unofficial supervisor Guillaume Backé for his invaluable help and guidance both in the field and throughout the year, even when he had a million more important things to do, I could not have completed this without him. Thanks to Justin Payne for all his help with the Hf isotope analysis work as well as providing invaluable comments on my draft. An enormous thankyou goes to the amazing staff at Adelaide Microscopy – especially Ben Wade and Angus Netting for their 24 hour commitment to keeping us and the machines happy, as well as Ken Neubauer for all the last minute carbon coating.

For making this project possible, I would like to thank the Australian Government for supporting this work through the Australia-India Strategic Research Fund along with the University of Adelaide. Thank you to the NGRI for their hospitality in Hyderabad. Thank you to Dilip Saha, Sarbani Patranabis Deb and their students from the ISI for their help and guidance in the field – especially Arnab and Paraijat for making sure we took extremely long lunch breaks and didn't work long hours in the field.

A massive thank you to my comrades also battling to understand the geological history of India - Bonnie Henderson, Andrew Barker, Ryan Gore and Georgy Falster, for being amazing fieldies, friends and endless pits of geological knowledge. To the entire Honours Class of 2011, thank you for making me smile, laugh, shudder, cringe and keeping me sane whilst sending me insane at the same time like only you guys could. To the amazing, zircon wizard, almost Dr, Katie Howard, thank you for all your help, support, wisdom and hilarity, the year would not have been the same without you.

I would like to thank my parents for their never ending emotional and financial support; I would not have had this opportunity without you. Lastly, thank you to Rondo who reminded me every day, without fail, that there's more to life than honours.

9.0 REFERENCES

ANAND M., GIBSON S. A., SUBBARAO K. V., KELLY S. P. & DICKIN A. P. 2003. Early Proterozoic melt generation processes beneath the intracratonic Cuddapah Basin, southern India. *J. Petrol* **44**, 2139-2171.

BELOUSOVA E. A., GRIFFIN W. L., O'REILLY S. Y. & FISHER N. I. 2002. Igneous zircon: trace element composition as an indicator of source rock type. *Contrib Mineral Petrol* **143**, 602-622.

CHALAPATHI RAO N. V., MILLER J. A., GIBSON S. A., PYLE D. M. & MADHAVAN V. 1999. Precise $^{40}Ar/^{39}Ar$ age determinations of the Kotakonda kimberlite and Chelima lamproite, India: implication for the mafic dyke swarm emplacement in the Eastern Dharwar craton. *Journal Geological Society of India* **53**, 425-432.

CHALAPATHI RAO N. V., MILLER J. A., PYLE D. M. & MADHAVAN V. 1996. New Proterozoic K-Ar ages for some kimberlites and lamproites from the Cuddapah basin and Dharwar craton, South India: evidence for non-contemporaneous emplacement. *Precambrian Research* **79**, 363-369.

CHATTERJEE N. & BHATTACHARJI S. 2001. Petrology, geochemistry and tectonic settings of the mafic dikes and sills associated with the evolution of the Proterozoic Cuddapah Basin of south India. *Journal of Earth System Science* **110**, 433.

CHAUDHURI A. K., SAHA D., DEB G. K., PATRANABIS DEB S., KANTI MUKHERJEE M. & GHOSH G. 2002. The Purana Basins of Southern Cratonic Province of India - A Case for Mesoproterozoic Fossil Rifts. *Gondwana Research* **5**, 23-33.

COLLINS A. S., SANTOSH M., BRAUN I. & CLARK C. 2007. Age and sedimentary provenance of the Southern Granulites, South India: U-Th-PbSHRIMP secondary ion mass spectrometry. *Precambrian Research* **155**, 125-138.

CRAWFORD A. R. & COMPSTON W. 1973. The age of the Cuddapah and Kurnool systems, southern India. *Journal of the Geological Society of Australia* **19**, 453-464.

DASGUPTA P. K. & BISWAS A. 2006. *Rhythms in Proterozoic Sedimentation: An Example From Peninsular India*. Satish Serial Publishing House, Delhi.

DASGUPTA P. K., BISWAS A. & MUKHERJEE R. 2005. 11. Cyclicity in Paleoproterozoic to Neoproterozoic Cuddapah Supergroup and its significance in basinal evolution. *In:* Jannes M. M. & Virgínio H. N. eds., *Developments in Sedimentology*, Vol. Volume 57, pp 313-354, Elsevier.

DOBMEIER C., LUTKE S., HAMMERSCHMIDT K. & MEZGER K. 2006. Emplacement and deformation of the Vinukonda meta-granite (Eastern Ghats, India) - Implications for the geological evolution of peninsular India and for Rodinia reconstructions. *Precambrian Research* **146**, 165-178.

DOBMEIER C. J. & RAITH M. M. 2003. Crustal Architecture and evolution of the Eastern Ghats Belt and adjacent regions of India. *Geological Society, London, Special Publications* **206**, 145-168.

FALSTER G. 2011. Geochronological and sedimentological constraints on the evolution of the lower Cuddapah Basin, India. The University of Adelaide (unpubl.).

FERRY J. & WATSON E. 2007. New thermodynamic models and revised calibrations for the Ti-in-zircon and Zr-in-rutile thermometers. *Contributions to Mineralogy and Petrology* **154**, 429-437.

FRENCH J. E. & HEAMAN L. M. 2010. Precise U–Pb dating of Paleoproterozoic mafic dyke swarms of the Dharwar craton, India: Implications for the existence of the Neoarchean supercraton Sclavia. *Precambrian Research* **183**, 416-441.

FRENCH J. E., HEAMAN L. M., CHACKO T. & SRIVASTAVA R. K. 2008. 1891–1883 Ma Southern Bastar–Cuddapah mafic igneous events, India: A newly recognized large igneous province. *Precambrian Research* **160**, 308-322.

FRIEND C. R. L. & NUTMAN A. P. 1991. SHRIMP U-PB Geochronology of the Closepet Granite and Peninsular Gneiss, Karnataka, South-India. *Journal of the Geological Society of India* **38**, 357-368.

GORE R. 2011. Geochronological and sedimentological constraints of the Srisailam Formation, S.E. India. The University of Adelaide (unpubl.).

GOSH D., DAS J. N., RAO A. K., RAY BARMAN T., KOLLAPURI V. K. & SARKAR A. 1994. Fission-track and K-Ar dating of pegmatite and associated rocks of Nellore schist belt, Andrah Pradesh: evidence of Middle to Late Proterozoic events. *Indian Minerals* **48**, 95-102.

GRIFFIN W. L., POWELL W. J., PEARSON N. J. & O'REILLY S. Y. 2008. GLITTER: data reduction software for laser ablation ICP-MS, Mineral. Assoc. Canada Short Course. *In:* Sylvester P. ed., *Laser Ablation-ICP-MS in the Earth Sciences: Current Practices and Outstanding Issues*, Vol. 40.

GRIFFIN W. L., WANG X., JACKSON S. E., PEARSON N. J., O'REILLY S. Y., XU X. & ZHOU X. 2002. Zircon chemistry and magma mixing, SE China: In-situ

analysis of Hf isotopes, Tonglu and Pingtan igneous complexes. *Lithos* **61**, 237-269.

HENDERSON B. J. 2011. The tectonic evolution of the Ongole Domain, India: A geochronological and metamorphic approach. The University of Adelaide (unpubl.).

HOWARD K. E., HAND M., BAROVICH K. M., REID A., WADE B. P. & BELOUSOVA E. A. 2009. Detrital zircon ages: Improving interpretation via Nd and Hf isotopic data. *Chemical Geology* **262**, 277-292.

IRELAND T. R., FLOTTMANN T., FANNING C. M., GIBSON G. M. & PREISS W. V. 1998. Development of the early Paleozoic Pacific margin of Gondwana from detrital-zircon ages across the Delamerian orogen. *Geology* **26**, 243-246.

JACKSON S. E., PEARSON N. J., GRIFFIN W. L. & BELOUSOVA E. A. 2004. The application of laser ablation-inductively coupled plasma-mass spectrometry to in situ U-Pb zircon geochronology. *Chemical Geology* **211**, 47-69.

JAYANANDA M., KANO T., PEUCAT J. J. & CHANNABASAPPA S. 2008. 3.35 Ga komatiite volcanism in the western Dharwar craton, southern India: Constraints from Nd isotopes and whole-rock geochemistry. *Precambrian Research* **162**, 160-179.

JAYANANDA M., MOYEN J. F., MARTIN H., PEUCAT J. J., AUVRAY B. & MAHABALESWAR B. 2000. Late Archaean (2550–2520 Ma) juvenile magmatism in the Eastern Dharwar craton, southern India: constraints from geochronology, Nd–Sr isotopes and whole rock geochemistry. *Precambrian Research* **99**, 225-254.

KAILASAM L. N. 1976. Geophysical studies of the major sedimentary basins of the indian craton, their deep structural features and evolution. *Tectonophysics* **36**, 225-241, 243, 245.

KALPANA G., MADHAVI T., PATIL D. J., DAYAL A. M. & RAJU S. V. 2010. Light gaseous hydrocarbon anomalies in the near surface soils of Proterozoic Cuddapah Basin: Implications for hydrocarbon prospects. *Journal of Petroleum Science and Engineering* **73**, 161-170.

KING W. 1872. Kudapah and Karnul Formations in the Madras Presidency. *Geological Survey of India*.

MACKINTOSH J. 2010. Age and Basin Evolution of the Cuddapah Supergroup, India. The University of Adelaide (unpubl.).

MANIKYAMBA C., KERRICH R., GONZÁLEZ-ÁLVAREZ I., MATHUR R. & KHANNA T. C. 2008. Geochemistry of Paleoproterozoic black shales from the Intracontinental Cuddapah basin, India: implications for provenance, tectonic setting, and weathering intensity. *Precambrian Research* **162**, 424-440.

MEERT J. G., PANDIT M. K., PRADHAN V. R., BANKS J., SIRIANNI R., STROUD M., NEWSTEAD B. & GIFFORD J. 2010. Precambrian crustal evolution of Peninsular India: A 3.0 billion year odyssey. *Journal of Asian Earth Sciences* **39**, 483-515.

MISHRA D. C. 2011. Long Hiatus in Proterozoic Sedimentation in India: Vindhyan, Cuddapah and Pakhal Basins - A Plate Tectonic Model. *Journal Geological Society of India* **77**, 17-25.

MUKHERJEE M. K. 2003. Very low-grade metamorphism vis-a-vis penetrative deformation in the southern Nallamalai fold-fault belt, Cuddapah basin, Andhra Pradesh. *Journal of the Geological Society of India* **62**, 535-548.

PEARCE N. J. G., PERKINS W. T., WESTGATE J. A., GORTON M. P., JACKSON S. E., NEAL C. R. & CHENERY S. P. 1997. A Compilation of New and Published

Major and Trace Element Data for NIST SRM 610 and NIST SRM 612 Glass Reference Materials. *Geostandards Newsletter* **21**, 115-144.

RAMAKRISHNAN M. & VAIDYANADHAN R. 2008. *Geology of India: Volume 1*.

SAHA D. 2002. Multi-stage deformation in the Nallamalai Fold Belt, Cuddapah basin, South India - Implications for Mesoproterozoic tectonism along southeastern margin of India. *Gondwana Research* **5**, 701-719.

SAHA D. & CHAKRABORTY S. 2003. Deformation pattern in the Kurnool and Nallamalai groups in the northeastern part (Palnad area) of the Cuddapah basin, South India and its implication on Rodinia/Gondwana tectonics. *Gondwana Research* **6**, 573-583.

SAHA D. & TRIPATHY V. 2011, In Review. *Paleoproterozoic Sedimentation in the Cuddapah Basin, south India and Regional Tectonics - a Review*.

SINGH A. P. & MISHRA D. C. 2002. Tectonosedimentary evolution of Cuddapah basin and Eastern Ghats mobile belt (India) as Proterozoic collision: gravity, seismic and geodynamic constraints. *Journal of Geodynamics* **33**, 249-267.

SINHA R. M., PARTHASARATHY T. N. & DWIVEDY K. K. 1995. On the Possibility of Identifying Low Cost, Medium Grade Uranium Deposits Close to the Proterozoic Unconformity in the Cuddapah Basin, Andhra Pradesh, India. *Department of Atomic Energy*.

SLAMA J., KOSLER J., CONDON D. J., CROWLEY J. L., GERDES A., HANCHAR J. M., HORSTWOOD M. S. A., MORRIS G. A., NASDALA L., NORBERG N., SCHALTEGGER U., SCHOENE B., TUBRETT M. N. & WHITEHOUSE M. J. 2008. Plesovice zircon - A new natural reference material for U-Pb and Hf isotopic microanalysis. *Chemical Geology* **249**, 1-35.

TAYLOR S. R. & MCLENNAN S. M. 1985. *The continental crust: its composition and evolution.* Blackwell, Oxford.

VASUDEVAN D., KRÖNER A., WENDT I. & TOBSCHALL H. 2003. Geochemistry, petrogenesis and age of felsic to intermediate metavolcanic rocks from the Palaeoproterozoic Nellore Schist Belt, Vinjamur, Andrah Pradesh, India. *Journal of Asian Earth Sciences*, in press.

VERVOORT J. D., PATCHETT P. J., BLICHERT-TOFT J. & ALBARÈDE F. 1999. Relationships between Lu–Hf and Sm–Nd isotopic systems in the global sedimentary system. *Earth and Planetary Science Letters* **168**, 79-99.

VERVOORT J. D., PATCHETT P. J., SÖDERLUND U. & BAKER M. 2004. Isotopic composition of Yb and the determination of Lu concentrations and Lu/Hf ratios by isotope dilution using MC-ICPMS. *Geochem. Geophys. Geosyst.* **5**, Q11002.

WATSON E., WARK D. & THOMAS J. 2006. Crystallization thermometers for zircon and rutile. *Contributions to Mineralogy and Petrology* **151**, 413-433.

WOODHEAD J., HERGT J., SHELLEY M., EGGINS S. & KEMP R. 2004. Zircon Hf-isotope analysis with an excimer laser, depth profiling, ablation of complex geometries, and concomitant age estimation. *Chemical Geology* **209**, 121-135.

10.0 TABLE CAPTIONS

Table 1: Summary of all analytical data collected from the Nallamalai Fold Belt including U-Pb geochronology, Hf isotope, REE and Ti-in-zircon thermometry data.

Table 2: Detailed descriptions of cathodoluminescence images of zircon grains from each sample.

Table 3: Chondrite normalised REE data for sample EA01

Table 4: Ti-in-zircon thermometry results for sample EA01 – Results for standards are highlighted yellow

Table 5: Chondrite normalised REE data for sample EA08

Table 6: Ti-in-zircon thermometry results for sample EA08 – Results for standards are highlighted yellow

11.0 FIGURE CAPTIONS

Figure 1: a) Regional setting of the Cuddapah Basin, Dharwar Craton, Eastern Ghats Belt and other Proterozoic basins of India, modified after French *et al.* (2008); b) Schematic map of the Cuddapah Basin with sub-basins representing stratigraphic groups, modified after Anand *et al.* (2003).

Figure 2: Stratigraphy of the Cuddapah Supergroup outlining previous and new constraints on age, modified after Anand *et al.* (2003).

Figure 3: Schematic map of the Nallamalai Group detailing sample locations, section lines and major localities. Modified after the Geological Survey of India (2011).

Figure 4: Detailed sequence of image interpretation showing the process undertaken to transform map view interpretation to cross section; a) Map view in Google Earth; b) 3D view of topography to interpret bedding topography relationships; c) Placement of interpreted bedding readings on the DEM along with further interpretation of faults and structure; d) Cross checking of structures in 3D Google Earth; e) Projection of interpreted structure onto geological sketch.

Figure 5: A regional structural map, overlain on a 90m resolution SRTM digital elevation model (DEM), outlining the main structures along the two section lines. The structural interpretation has been made from analysis of the DEM and the 15m resolution Landsat 7 ETM images and completed by field observations. The transect lines of the two geological sketch lines are shown on the map.

Figure 6: a) Trace of Section I across the SRTM DEM; b) Interpreted geological sketch across the entire Cuddapah Basin and into the Nellore Schist Belt incorporating work previously completed by Mackintosh (2010); c) Geological sketch along Section I depicting the main structural features of the NFB, specifically in terms of the contact between the Nallamalai Group and Kurnool Group.

Figure 7: a) Trace of Section II across the SRTM DEM; b) Geological sketch along Section II depicting the main structural features across the contact between the Nallamalai Group and Srisailam Formation as well as the Iswarakuppam Dome.

Figure 8: a-g) U-Pb probability density diagrams for all detrital zircon geochronology results showing both 90-110% concordant data as well as discordant data; h) All data

from the Nallamalai Group plotted as one probability density diagram. All plots are marked with 1700 - 1900 Ma and 2400 - 2600 Ma marker bands to show the abundance of zircon grains recording these ages.

Figure 9: Conventional U-Pb concordia diagrams for samples EA01, EA04, EA05 and EA06, maximum depositional ages for each sample are labelled. Inset: representative CL image of a zircon grain from respective sample.

Figure 10: Conventional U-Pb concordia diagrams for samples EA07, EA08 and CU10-09, maximum depositional ages for each sample are labelled. Inset: representative CL image of a zircon grain from respective sample.

Figure 11: ε_{Hf} isotope data from samples EA01, EA04, EA05, EA08 and CU10-09 - ε_{Hf} values are plotted against U-Pb age for individual zircons from the Nallamalai Group.

Figure 12: Initial $^{177}Hf/^{176}Hf$ data from samples EA01, EA04, EA05, EA08 and CU10-09 plotted against U-Pb geochronology – allowing $T_{(DM)\ (crustal)}$ model ages to be calculated. Ages are calculated using an average crustal composition of $^{176}Lu/^{177}Hf=0.015$.

Figure 13: Chondrite normalised REE zircon data for samples EA01 and EA08 overlain on Fields of Zircon Composition plots produced by Belousova *et al.* (2002), all values were normalised using the chondrite normalisation values of Taylor & McLennan (1985). a) Y vs U; b) Y vs Yb/Sm; c) Y vs Ce/Ce*; d) Ce/Ce* vs Eu/Eu*.

Figure 14: Chondrite normalised REE values for sample EA01 where chondrite normalised values are plotted against the respective element creating a “signature”

for each zircon analysed. Inset: Average REE signatures for different rock types as of Belousova *et al.* (2002).

Figure 15: Chondrite normalised REE values for sample EA08 where chondrite normalised values are plotted against the respective element creating a “signature” for each zircon analysed. Inset: Average REE signatures for different rock types as of Belousova *et al.* (2002).

12.0 TABLES

	U/Pb Geochronology			*Hf Isotope Analysis*			*REE composition*			
Sample Name	**No. Of Analyses - concordant/total**	**207Pb/206Pb Max. Dep. Age(Ma)**	**Age Peaks (Ma)**	**ε_{Hf} (range)**	**$T_{DM\ (crustal)}$ (range)**	**Total REE**	**LREE (Ave.)**	**HREE (Ave.)**	**Ce anomaly (Ave.)**	**Ti-in-zircon**
EA01	63/108	1882 ± 22	2935, **2525,** 2345	-11 to +3	2.85 - 3.46	1575	7.68	39.48	6.34	872 ± 30
EA04	68/90	1682 ± 25	3316, 2757, **2489,** 2031, 1875	-10 to +6	2.6 - 3.5	-	-	-	-	-
EA05	48/85	1661 ± 20	2715, 2360, **2499,** 2007, 1910, 1844, 1767	-23 to -3	3.14 - 3.89	-	-	-	-	-
EA06	9/17	1843 ± 32	2604, **2515**, 2465	-	-	-	-	-	-	-
EA07	65/80	1783 ± 71	2666, **2470**, 1850	-	-	-	-	-	-	-
EA08	71/80	1836 ± 20	2689, **2515**, 2310, 2200, 1890	-15 to +6	2.73 - 3.85	1917	25.05	34.99	9.01	906 ± 36
CU10-09	58/96	1774 ± 21	3074, **2538**, 2098, 1850	-14 to +3	2.45 - 3.15	-	-	-	-	-

Table 1

Sample	*Location*	*Size (µm)*	*Colour*	*A.R.*	*CL Description*
EA01	16˚05'41.1"N 79˚41'40.6"E	50 - 300	Reddish-pink to pale yellow	1:1.5	Large cores with minimal rims, zoning ranging from oscillatory to minimal.
EA04	15˚34'41.9"N 79˚18'06.4"E	50 - 150	Pale orange to pale yellow	1:2	Large cores, minimal rims, bright oscillatory zoning
EA05	15˚25'37.5"N 78˚45'42.1"E	50 - 150	Dark-pink to orange	1:2	Large cores with obvious oscillatory zoning
EA06	15˚11'12.0"N 78˚38'01.8"E	50 - 100	Pink to yellow	1:2.5	Large cores with dull oscillatory zoning, very few rims
EA07	15˚41'25.0"N 79˚09'59.8"E	50 - 150	Clear to pale yellow	1:2.5	Small to large oscillatory zoned cores with some to no overprinting rims
EA08	15˚45'43.5"N 79˚12'29.2"E	100 - 200	Pinkish red to yellow to clear	1:1.5	Large oscillatory zoned cores, minimal rims.
CU10-09	15˚23'34.2"N 78˚39'48.3"E	40 - 100	Pale orange to pale yellow	1:1.5	Large cores with minimal overprinting rims, oscillatory zoning.

Table 2

Sample EA01

Element	ree03	ree05	ree06	ree07	ree15	ree16	ree17	ree22	ree24	ree27	ree36	ree38	ree40	ree41	ree42	ree43	ree58
La139	1.234332	22.6158	83.32425	324.6866	29.70027	11.66213	59.23706	43.13351	8.092643	99.48229	53.48774	3.395095	1.392371	225.2861	1.689373	33.07902	24.44142
Ce140	34.49321	70.44932	163.0094	455.8203	77.16823	32.72727	112.1944	76.72936	52.85266	112.4974	164.9425	21.75549	101.6614	282.4138	18.10867	72.45559	102.1526
Pr141	2.540146	37.81022	124.8905	375.9124	41.82482	9.40146	42.48175	47.59124	13.86861	57.66423	98.0292	1.59854	4.116788	265.9854	4.693431	32.48175	38.90511
Nd146	4.824191	42.18003	141.5752	387.8622	53.23488	15.13361	41.23769	56.01969	19.71871	53.33333	108.4669	3.206751	12.40506	267.3136	11.06892	35.89311	53.09423
Sm147	20.30303	67.48918	187.6623	395.4113	195.8874	25.02165	60.82251	101.0823	63.85281	77.61905	164.5022	14.71861	61.16883	261.4286	44.11255	44.97835	167.7922
Eu153	15.86207	60.22989	211.7241	277.0115	291.6092	19.54023	41.72414	71.83908	54.48276	47.93103	148.5057	13.93103	52.29885	191.2644	19.85057	33.56322	88.3908
Gd157	79.37908	118.8562	270.8824	516.732	530.2614	81.24183	133.3007	278.2026	179.902	142.7451	271.7974	53.59477	194.7386	435.5556	133.0392	95.29412	340.7843
Tb159	146.7241	182.069	357.931	597.069	645.6897	125.3448	212.931	477.7586	273.4483	207.931	369.3103	94.13793	319.4828	591.7241	217.2414	151.5517	490.8621
Dy163	271.6798	274.5669	503.832	736.0367	810.4987	210.7349	362.1522	786.7979	419.1864	330.6299	503.4121	175.4068	553.7008	883.4908	362.2572	248.8189	808.9764
Ho165	488.6016	423.1492	731.1398	928.7897	986.7215	348.0611	597.6498	1142.773	629.1422	492.5969	705.7579	296.9448	897.6498	1310.576	565.4524	407.168	1188.014
Er166	804.498	639.7189	1053.655	1233.253	1230.321	520	962.2088	1594.94	891.0843	695.5422	1078.675	490.6024	1331.325	1851.004	797.6305	657.1486	1664.498
Tm169	1368.82	1097.191	1761.517	1960.955	1757.022	808.1461	1691.011	2463.764	1364.888	1074.719	1733.427	875	2101.124	2778.933	1219.944	1164.045	2906.742
Yb172	2023.306	1756.411	2708.911	2854.556	2383.508	1083.831	2677.944	3565.161	1905.363	1537.661	2567.5	1418.79	2977.54	3975.605	1687.419	1852.903	3952.621
Lu175	2518.11	1840.157	2881.89	2774.541	2479.265	1314.961	3037.27	3546.194	2001.575	1540.682	3664.829	1502.1	3101.837	4226.772	1670.604	2038.583	3631.496
LREE	16.44859	2.98416	2.252194	1.217824	6.595476	2.145548	1.026765	2.343474	7.89023	0.78023	3.075512	4.335258	43.93143	1.160429	26.11179	1.359725	6.865077
HREE	124.0263	27.26596	15.35678	7.016848	12.65658	52.55292	49.93662	35.08226	31.3467	19.84928	22.27831	102.0544	50.70944	16.16798	37.87139	45.32364	21.64282
Ce/Ce*	19.47997	2.409163	1.597946	1.304722	2.189482	3.125527	2.236521	1.693521	4.988904	1.485307	2.277864	9.338584	42.46192	1.153692	6.431001	2.210425	3.312705

Table 3

Spot	Ti49	Error	T (K)	T (C)	σd	σT	U/Pb Age
NIST610a	432.36	19.25	1560.675	1287.675	0.075697	47.51562	
NIST610b	455.16	21.73	1572.087	1299.087	0.075764	48.12002	
NIST610d	430.6	21.83	1559.777	1286.777	0.076212	47.68171	
NIST610E	438.12	22.69	1563.598	1290.598	0.076228	47.88224	
NIST610f	384.83	22.22	1535.419	1262.419	0.077327	46.89997	
NIST610g	375.6	22.14	1530.256	1257.256	0.077563	46.73251	
ree03	23.25	3.27	1104.604	831.6038	0.19302	52.91532	2522.9
ree05	31.6	2.88	1139.565	866.5652	0.143093	43.77356	2500.3
ree06	64.38	5.03	1229.838	956.838	0.107788	40.49105	2374.3
ree07	44.19	3.14	1180.394	907.3936	0.117087	40.03577	2484.8
ree15	47.92	3.74	1190.702	917.7024	0.117555	40.75766	2485.1
ree16	16.31	3.16	1066.79	793.7896	0.261085	64.79694	2520.9
ree17	16.09	2.5	1065.392	792.3925	0.237451	59.3171	2536
ree22	13.98	2.75	1051.143	778.1433	0.282464	67.70554	2381.6
ree24	26.53	2.51	1119.374	846.3736	0.155214	45.21632	2444.3
ree27	20.45	2.92	1090.611	817.6112	0.205434	54.53735	2555.9
ree36	34.65	3.63	1150.499	877.4994	0.14565	45.15205	2552.7
ree38	10.3	2.18	1021.454	748.4541	0.337832	75.69564	2532
ree40	27.57	2.36	1123.752	850.7517	0.147124	43.63662	2520.9
ree41	38.75	2.74	1164.056	891.0557	0.121896	40.2435	2916.3
ree42	23.13	2.18	1104.033	831.0326	0.163671	46.03633	2172.9
ree43	12.05	1.84	1036.492	763.4923	0.269016	63.02109	2457.4
ree58	35.53	6.1	1153.512	880.512	0.175509	52.86854	2421.3

Table 4

Sample EA08

Element	ree01	ree02	ree03	ree04	ree06	ree13	ree15	ree23	ree29	ree30	ree33	ree37	ree62	ree63	ree64	ree67	ree73
La139	263.2153	11.38965	64.16894	0.594005	6.430518	1.953678	2.40327	44.95913	44.95913	25.58583	1.553134	144.9864	25.04087	164.6594	13.73297	0.446866	0.392371
Ce140	262.4451	105.3605	269.8537	56.76071	24.03344	9.477534	62.63323	102.0376	107.2205	149.0178	46.01881	691.7868	88.36991	341.139	40.55381	14.09613	13.1139
Pr141	241.0219	25.0365	137.7372	2.313869	14.9635	3.905109	7.124088	37.44526	32.11679	46.27737	4.153285	300.8759	48.10219	192.6277	22.26277	2.729927	0.832117
Nd146	251.1533	33.51617	208.1997	5.288326	17.48242	8.706048	11.72996	51.96906	35.68214	63.3474	8.649789	372.9114	63.90999	224.3601	32.29255	8.635724	3.361463
Sm147	311.2554	103.3333	426.6234	33.20346	54.11255	56.79654	42.51082	212.1212	59.26407	189.0043	29.39394	811.5152	235.368	381.9481	93.29004	87.09957	21.25541
Eu153	124.2529	112.069	460.4598	12.06897	60.57471	29.65517	32.87356	304.8276	111.8391	189.4253	39.77011	821.954	304.8276	361.7241	91.49425	136.092	15.09195
Gd157	477.5817	253.4641	596.6667	123.8235	148.6601	253.6928	117.6144	780.3595	113.7255	380.6863	82.9085	1089.542	644.183	541.0458	208.4641	360.098	107.8758
Tb159	641.3793	373.2759	694.6552	239.6552	307.7586	558.6207	211.2069	976.8966	149.1379	547.5862	134.4828	1186.207	860	686.2069	326.2069	506.0345	203.4483
Dy163	938.6877	550.8399	794.3832	463.3858	357.5066	1132.835	345.5381	1279.869	216.4042	785.5118	223.5171	1295.407	992.5459	841.5223	473.4646	652.7034	371.4698
Ho165	1248.884	821.3866	1006.58	773.678	311.7509	1952.174	564.2773	1569.683	318.6839	1138.308	359.1069	1488.132	1153.467	1126.557	617.3913	746.181	608.2256
Er166	1775.261	1151.165	1354.9	1197.871	293.8554	2997.55	853.8153	1985.622	471.004	1688.835	566.1446	1893.414	1431.165	1570.643	826.3454	850.4819	901.2851
Tm169	2430.899	1646.91	2262.36	1819.101	359.2697	4957.303	1376.966	2475.843	788.4831	2706.742	937.0787	2707.584	1959.27	2273.596	1163.483	1221.629	1384.27
Yb172	3118.952	2239.677	3402.984	2497.863	442.7016	7091.976	2010.685	3070.403	1166.694	3910.645	1383.629	3767.177	2486.976	3052.056	1523.589	1563.105	2002.016
Lu175	3665.092	2641.732	4617.848	3040.42	439.895	6355.118	2001.575	3427.034	1475.591	5123.36	1691.864	4513.648	2958.268	3943.045	1790.289	1511.286	2067.192
LREE	1.182513	9.072568	6.648441	55.89757	8.414961	29.07159	17.68874	4.71809	1.318177	7.38707	18.92557	5.597182	9.399352	2.319625	6.793144	194.9118	54.17178
HREE	11.77519	25.56515	10.82418	91.56936	8.12926	111.8927	47.08389	16.15602	24.89857	27.1071	57.55824	5.562001	12.56869	10.32351	19.19057	17.35125	97.25484
Ce/Ce*	1.041969	6.239301	2.870386	48.41537	2.450058	3.431249	15.13697	2.486869	2.821647	4.330658	18.11904	3.312188	2.546228	1.915485	2.319316	12.7625	22.95046

Table 5

Analysis	Ti49	Error	T (K)	T (°c)	σd	σT	U/Pb age
NIST610a	410.63	20.76	1549.39	1276.39	0.076399	47.23308	
NIST610b	412.75	21.62	1550.51	1277.51	0.07653	47.34281	
NIST610d	437.48	22.4	1563.275	1290.275	0.076187	47.84903	
NIST610e	448.63	23.15	1568.861	1295.861	0.076117	48.10362	
NIST610f	422.65	23.15	1555.684	1282.684	0.076623	47.64285	
NIST610g	425.89	23.37	1557.359	1284.359	0.076597	47.71724	
ree01	27.1	5.59	1121.79	848.7897	0.2134	59.45807	2689.5
ree02	42.58	5.37	1175.732	902.7316	0.144525	46.65559	2439.2
ree03	78.15	7.51	1256.957	983.9575	0.108183	42.13796	2446.5
ree04	30.93	4.78	1137.052	864.0518	0.177975	52.09563	1912.8
ree06	30.15	5.88	1134.071	861.0707	0.198694	56.99359	1995.5
ree13	35.96	6.1	1154.963	881.9627	0.173766	52.54556	1926.8
ree15	24.49	3.31	1110.372	837.3722	0.185592	51.66457	2541.1
ree23	38.34	3.88	1162.753	889.7526	0.138487	44.22801	2688.1
ree29	17.06	2.32	1071.441	798.4409	0.217824	55.52994	2318.8
ree30	28.51	3.18	1127.597	854.597	0.161018	47.20237	2482
ree33	13.72	2.91	1049.269	776.2691	0.295206	70.28591	2529.3
ree37	57.67	5.81	1214.953	941.9526	0.120192	42.90116	2442.1
ree54	79.17	6.22	1258.815	985.8146	0.102203	40.5889	2716.5
ree62	72.65	5.13	1246.608	973.6077	0.101672	39.78401	2574.7
ree63	96.53	9.29	1287.906	1014.906	0.102323	42.22726	2212.1
ree64	31.89	4.41	1140.64	867.64	0.167855	49.88479	1854.9
ree67	28.39	3.62	1127.112	854.1117	0.170284	49.39347	2472
ree73	10.75	2.07	1025.509	752.5087	0.316471	71.74553	2584.9

Table 6

13.0 FIGURES

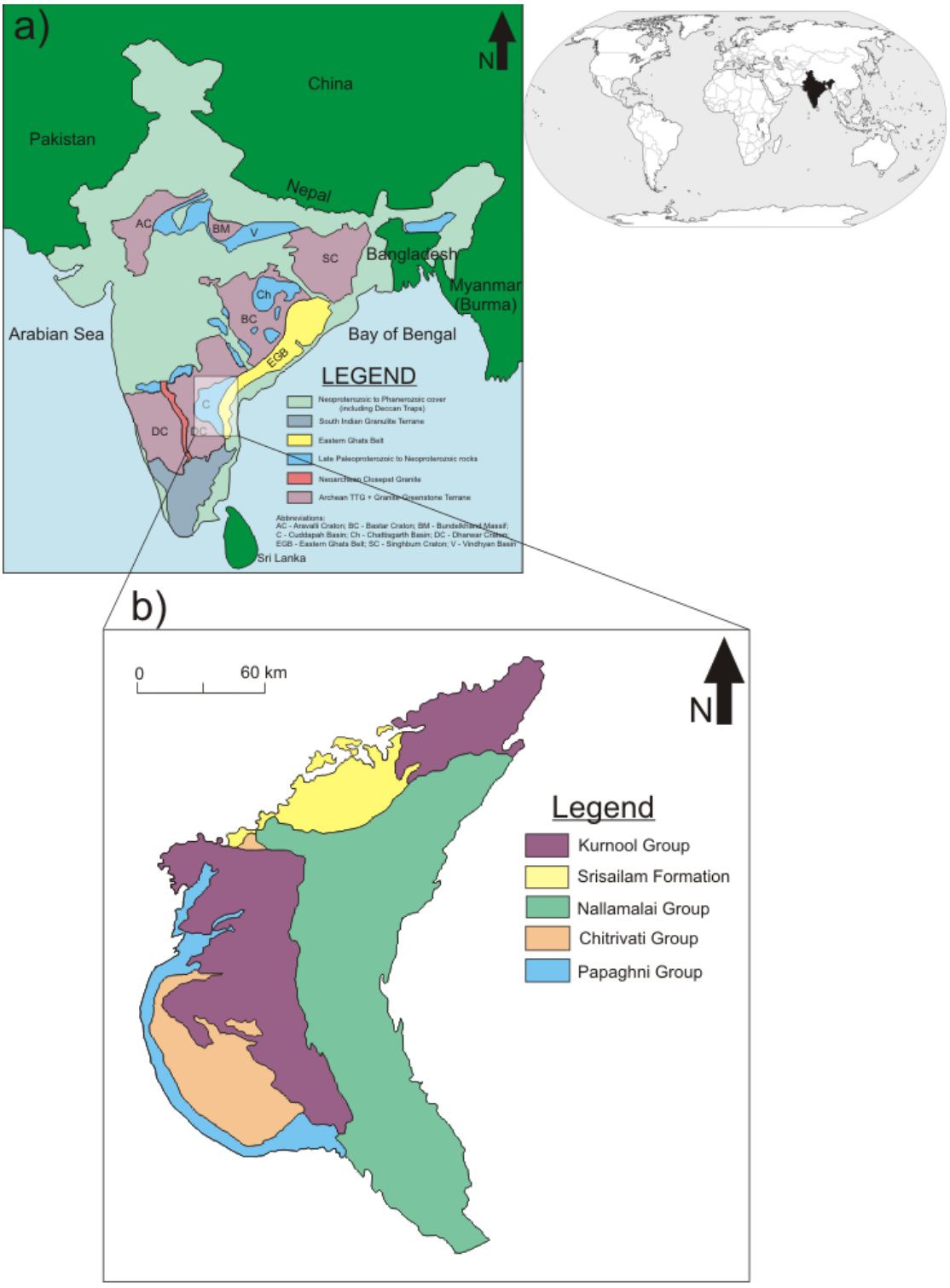

Figure 1

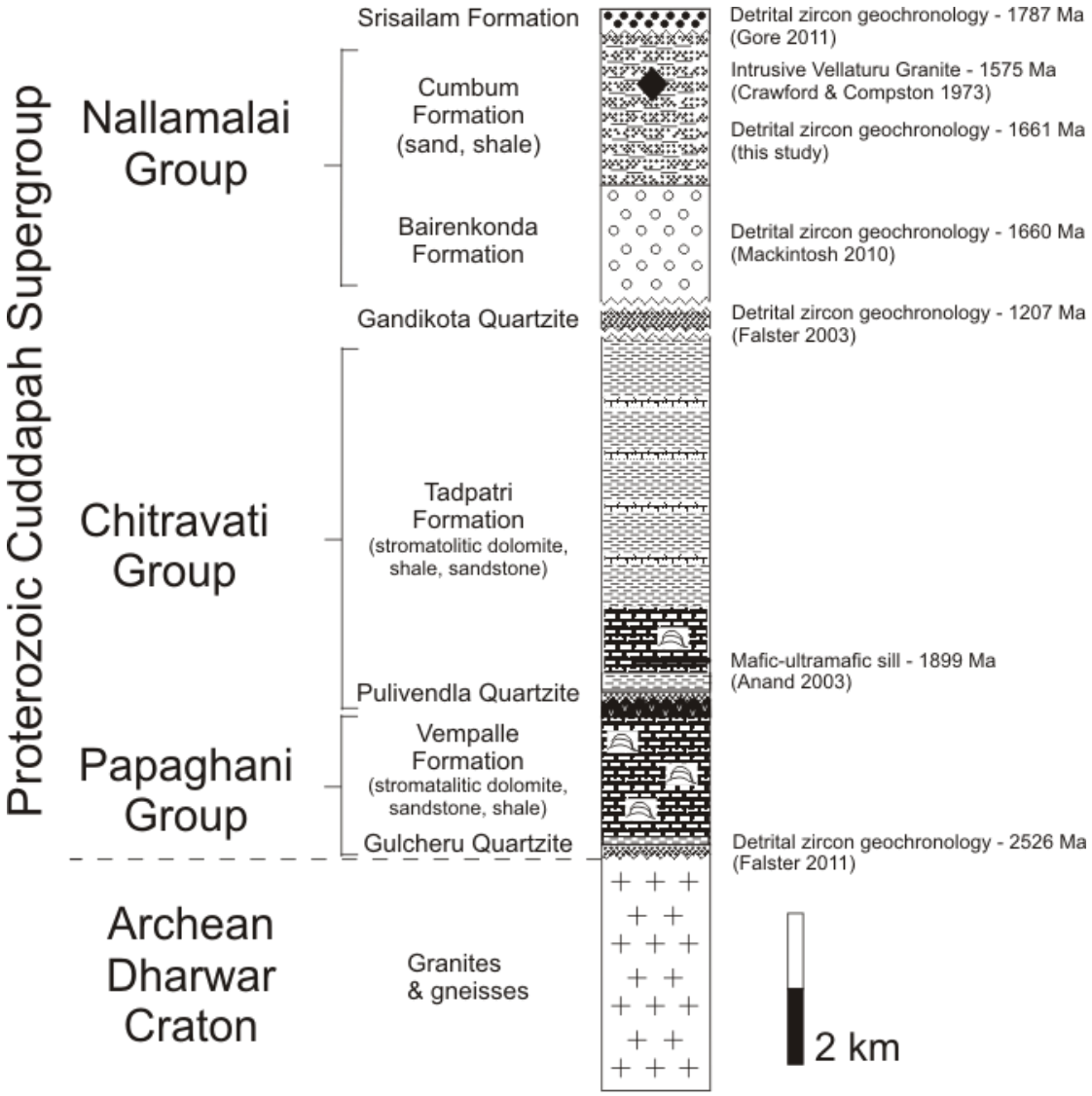
Proterozoic Cuddapah Supergroup
Nallamalai Group
Chitravati Group
Papaghani Group
Archean Dharwar Craton
Srisailam Formation
Cumbum Formation (sand, shale)
Bairenkonda Formation
Gandikota Quartzite
Tadpatri Formation (stromatolitic dolomite, shale, sandstone)
Pulivendla Quartzite
Vempalle Formation (stromatalitic dolomite, sandstone, shale)
Gulcheru Quartzite
Granites & gneisses
Detrital zircon geochronology - 1787 Ma (Gore 2011)
Intrusive Vellaturu Granite - 1575 Ma (Crawford & Compston 1973)
Detrital zircon geochronology - 1661 Ma (this study)
Detrital zircon geochronology - 1660 Ma (Mackintosh 2010)
Detrital zircon geochronology - 1207 Ma (Falster 2003)
Mafic-ultramafic sill - 1899 Ma (Anand 2003)
Detrital zircon geochronology - 2526 Ma (Falster 2011)
2 km

Figure 2

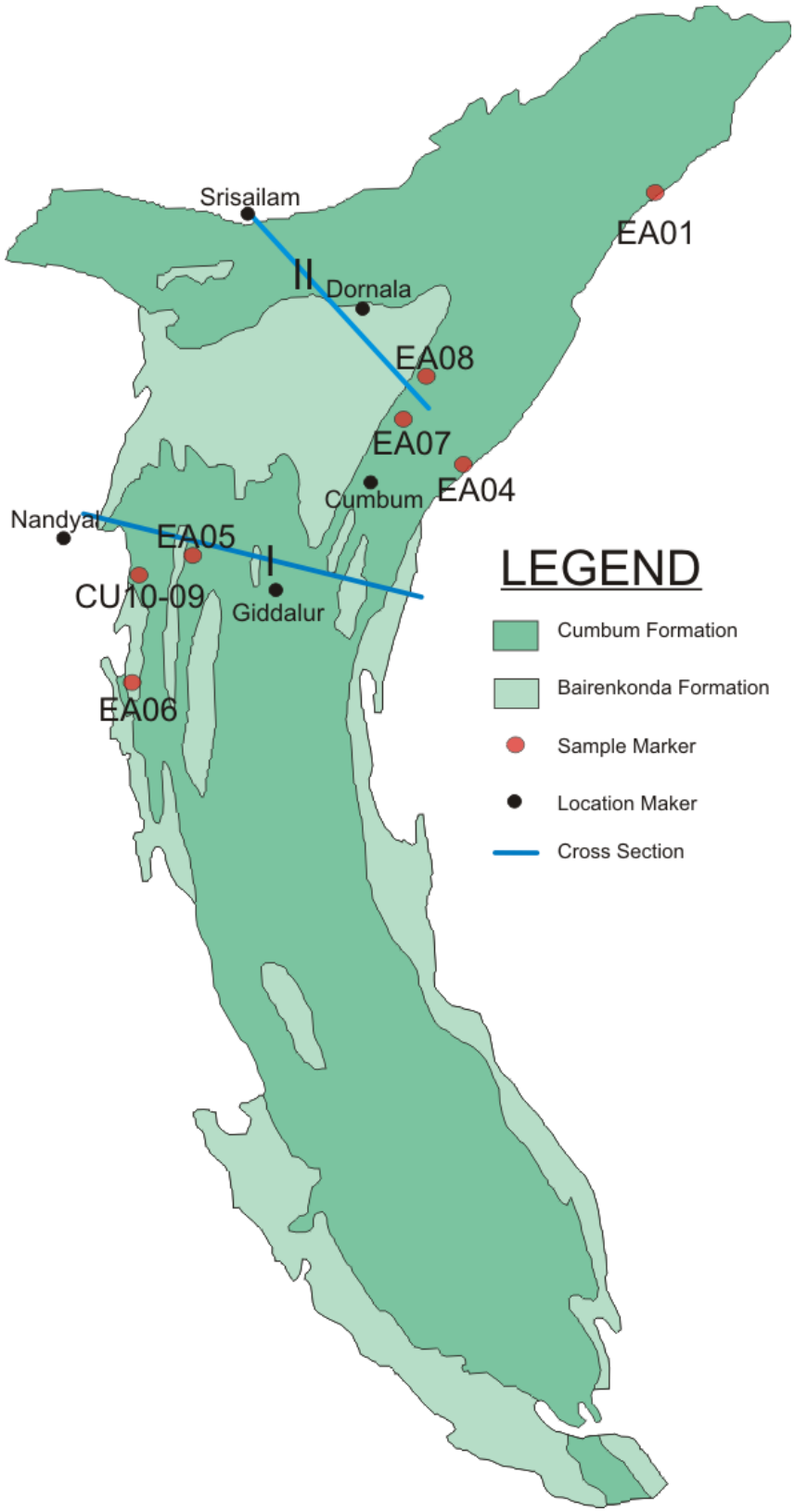
Srisailam
II
Dornala
EA01
EA08
EA07
EA04
Cumbum
Nandyal
EA05
I
CU10-09
Giddalur
EA06
LEGEND
Cumbum Formation
Bairenkonda Formation
Sample Marker
Location Maker
Cross Section

Figure 3

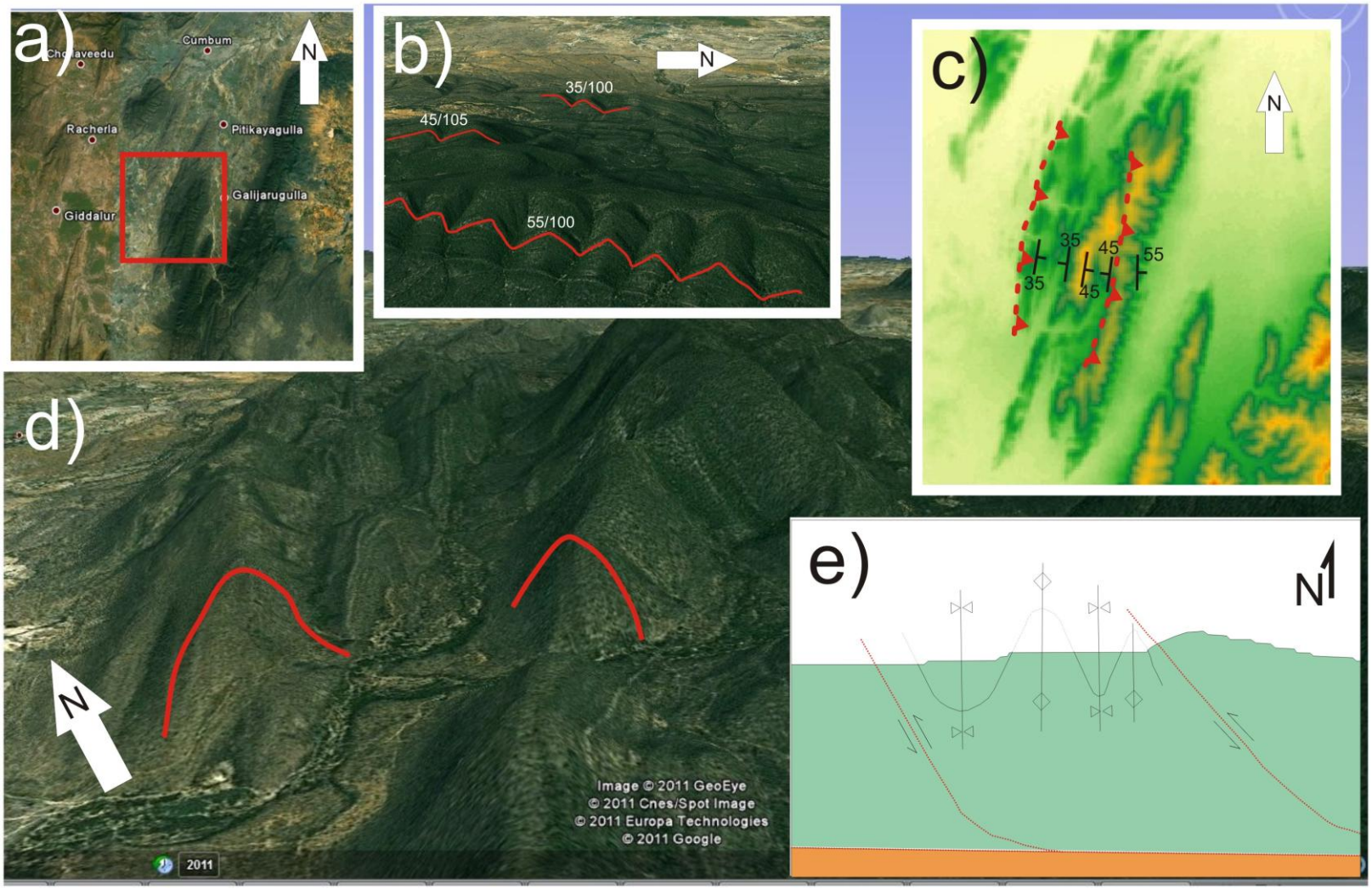
a)
Cumbum
Racherla
Pitikayagulla
Galijarugulla
Giddalur
N
b)
35/100
45/105
55/100
N
c)
N
35
45
55
35
45
d)
N
Image © 2011 GeoEye
© 2011 Cnes/Spot Image
© 2011 Europa Technologies
© 2011 Google
2011
e)
N

Figure 4

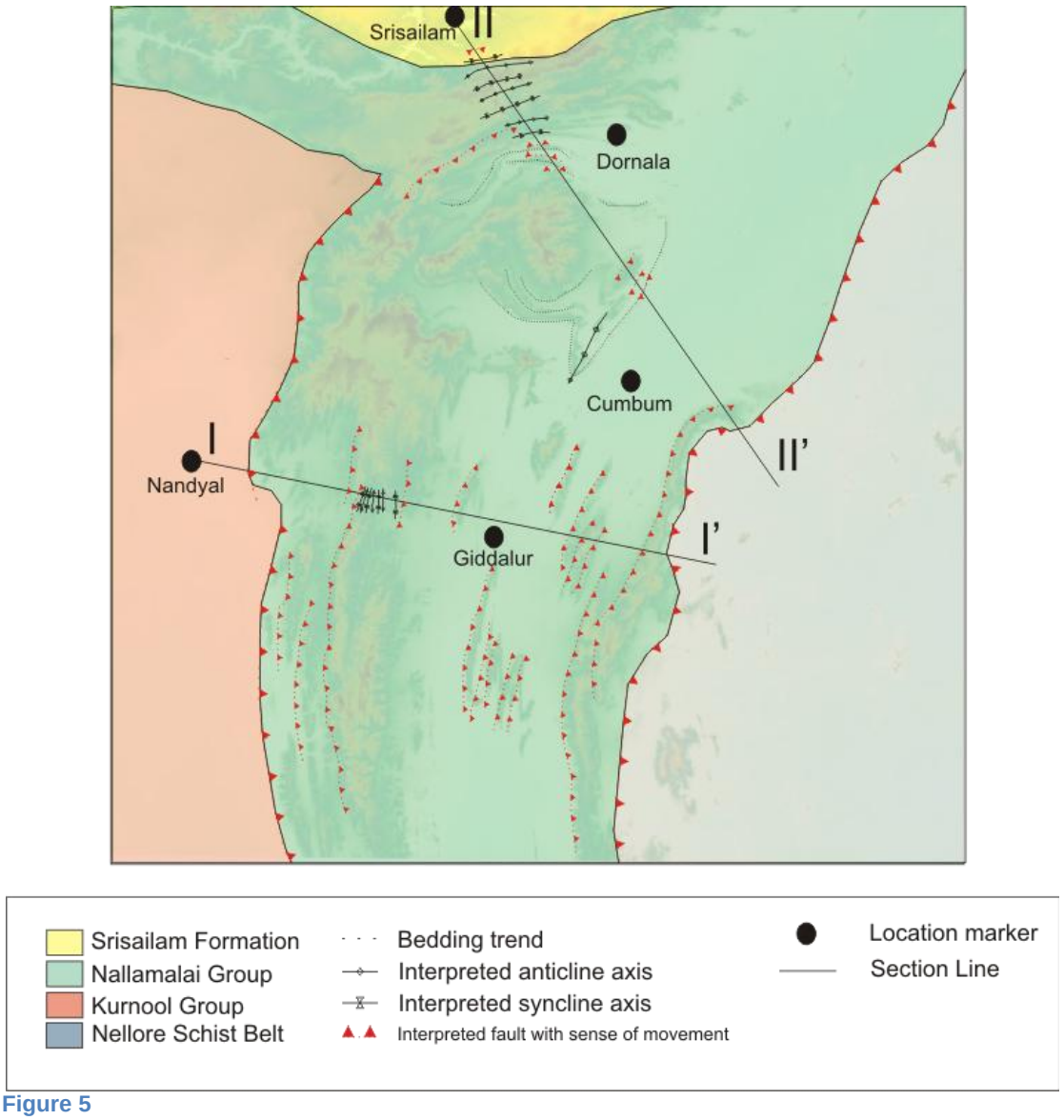
Srisailam
II
Dornala
Cumbum
II'
I
Nandyal
I'
Giddalur
Srisailam Formation
Nallamalai Group
Kurnool Group
Nellore Schist Belt
Bedding trend
Interpreted anticline axis
Interpreted syncline axis
Interpreted fault with sense of movement
Location marker
Section Line

Figure 5

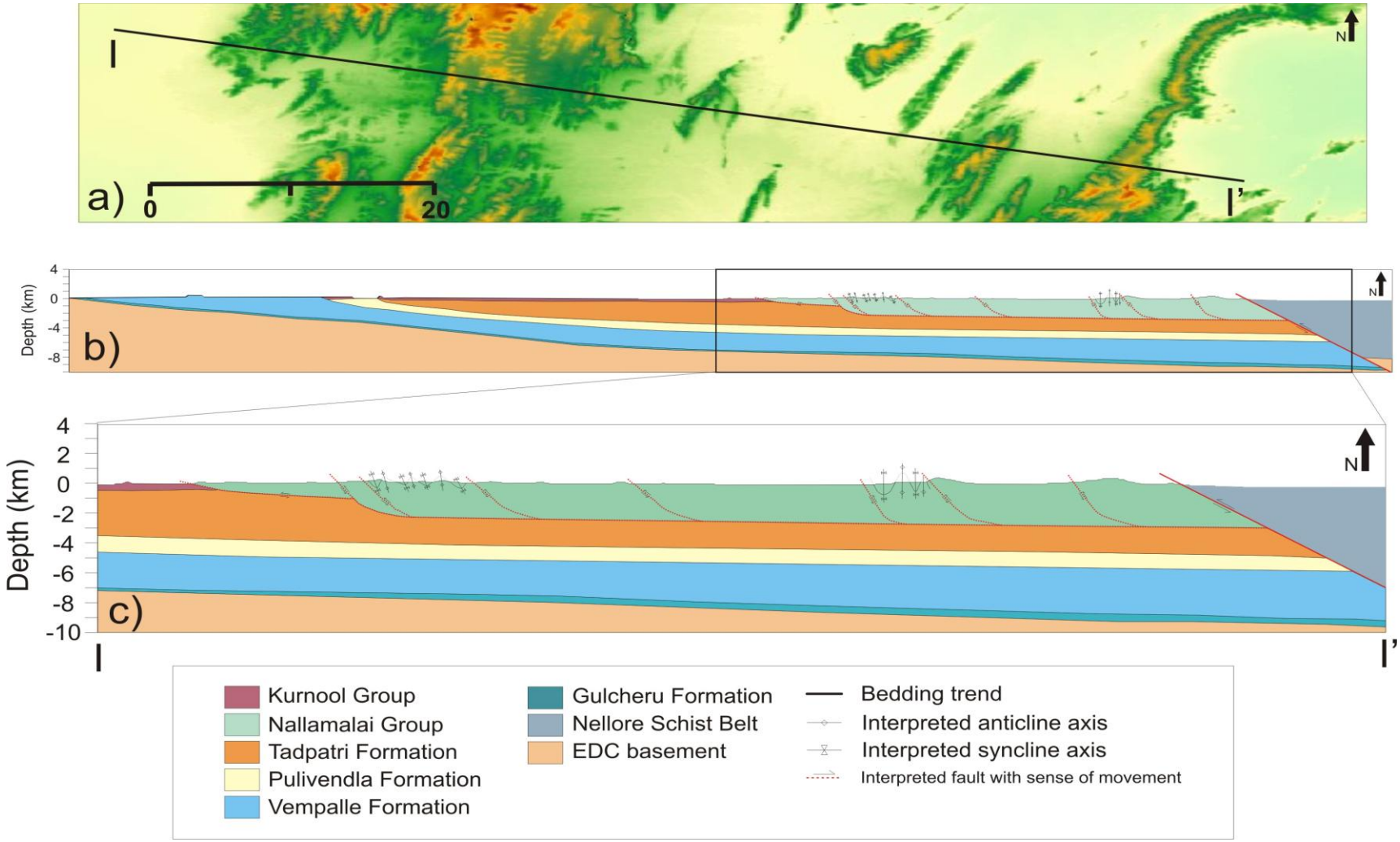
a)
0
20
l
l'
N
b)
Depth (km)
4
0
-4
-8
c)
4
2
0
-2
-4
-6
-8
-10
Kurnool Group
Nallamalai Group
Tadpatri Formation
Pulivendla Formation
Vempalle Formation
Gulcheru Formation
Nellore Schist Belt
EDC basement
Bedding trend
Interpreted anticline axis
Interpreted syncline axis
Interpreted fault with sense of movement

Figure 6

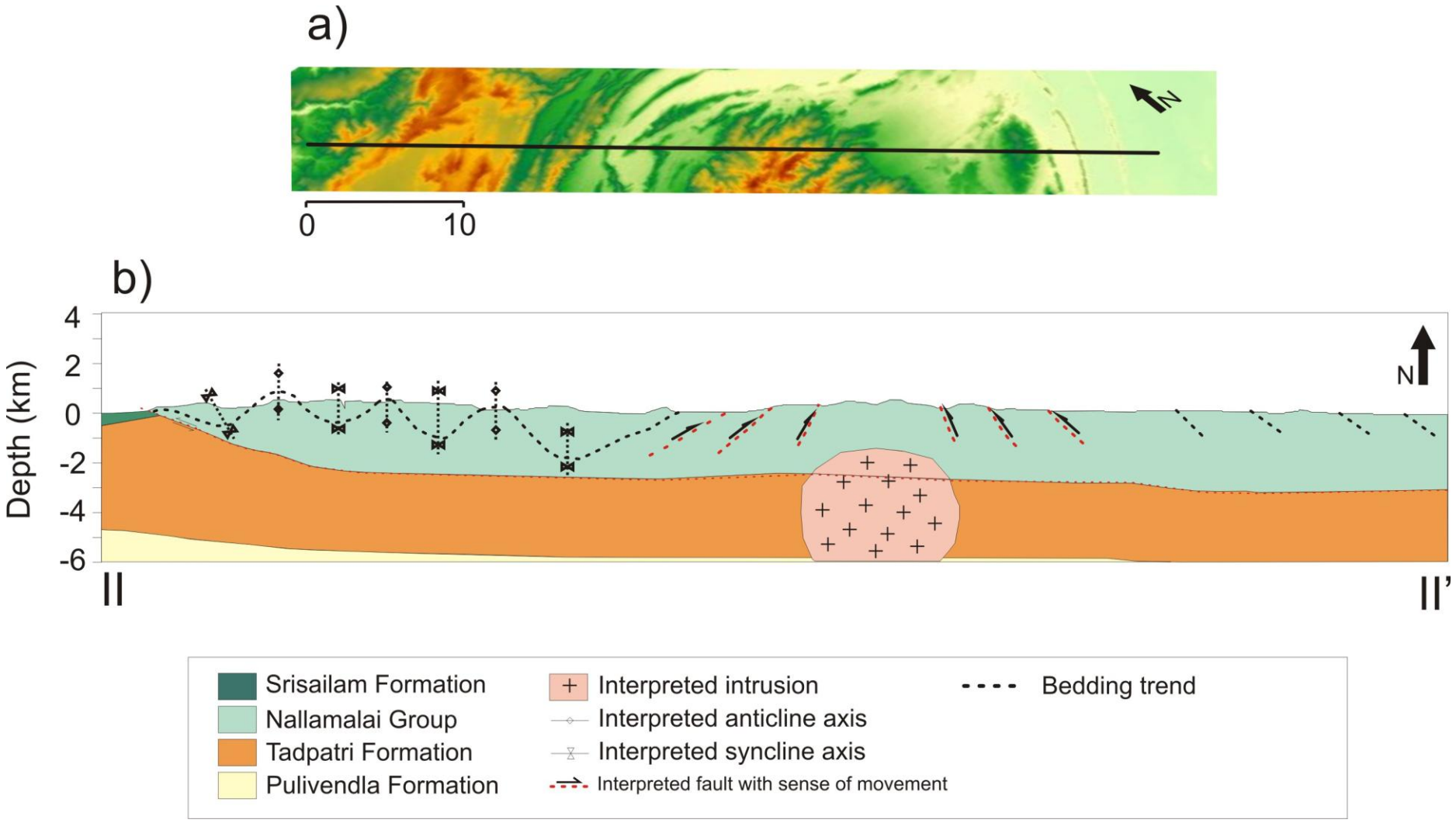
a)
N
0
10
b)
Depth (km)
4
2
0
-2
-4
-6
N
II
II'
Srisailam Formation
Nallamalai Group
Tadpatri Formation
Pulivendla Formation
Interpreted intrusion
Interpreted anticline axis
Interpreted syncline axis
Interpreted fault with sense of movement
Bedding trend

Figure 7

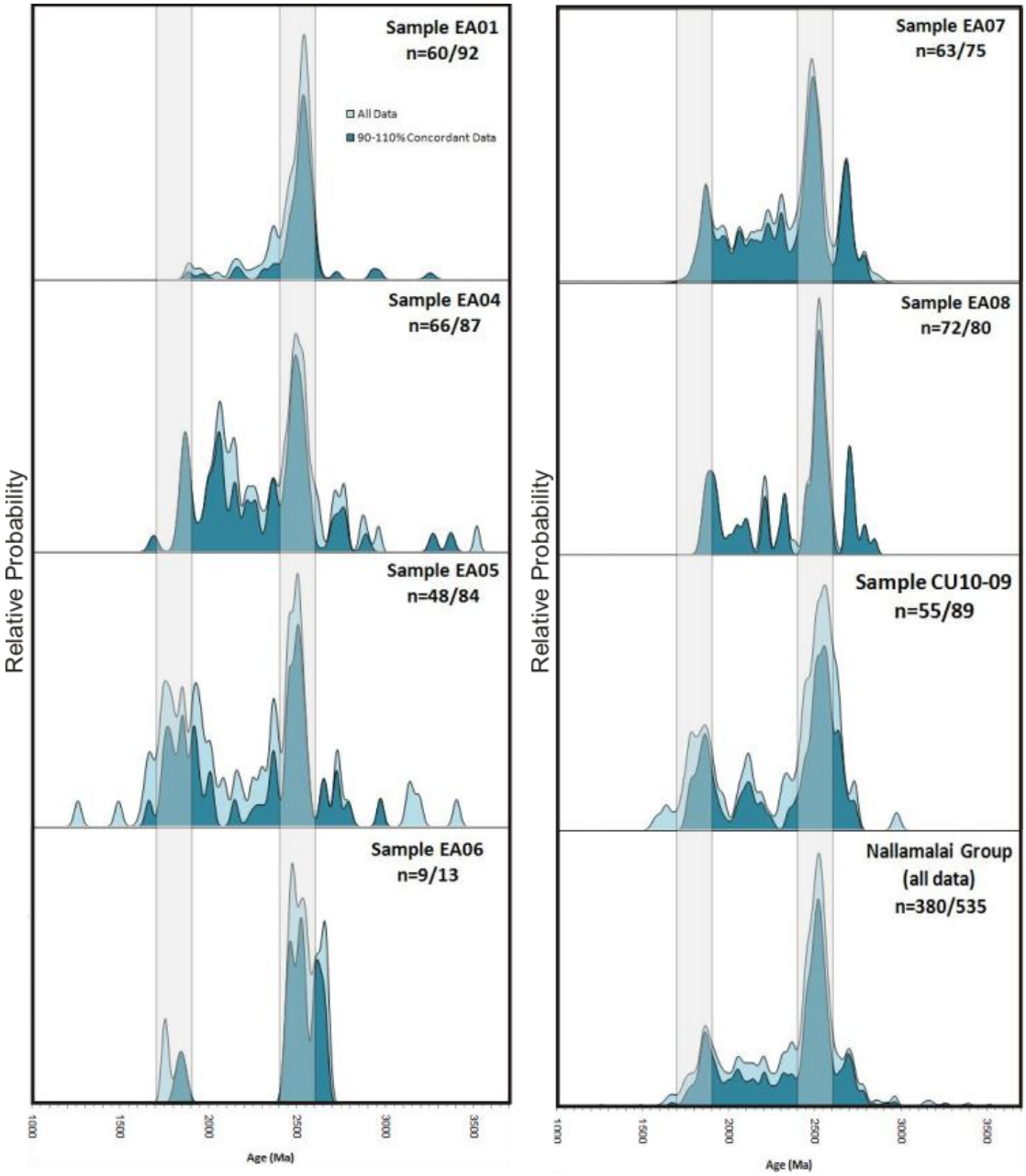
Sample EA01
n=60/92
All Data
90-110% Concordant Data
Sample EA04
n=66/87
Sample EA05
n=48/84
Sample EA06
n=9/13
Relative Probability
1000
1500
2000
2500
3000
3500
Age (Ma)
Sample EA07
n=63/75
Sample EA08
n=72/80
Sample CU10-09
n=55/89
Nallamalai Group
(all data)
n=380/535
Relative Probability
1000
1500
2000
2500
3000
3500
Age (Ma)

Figure 8

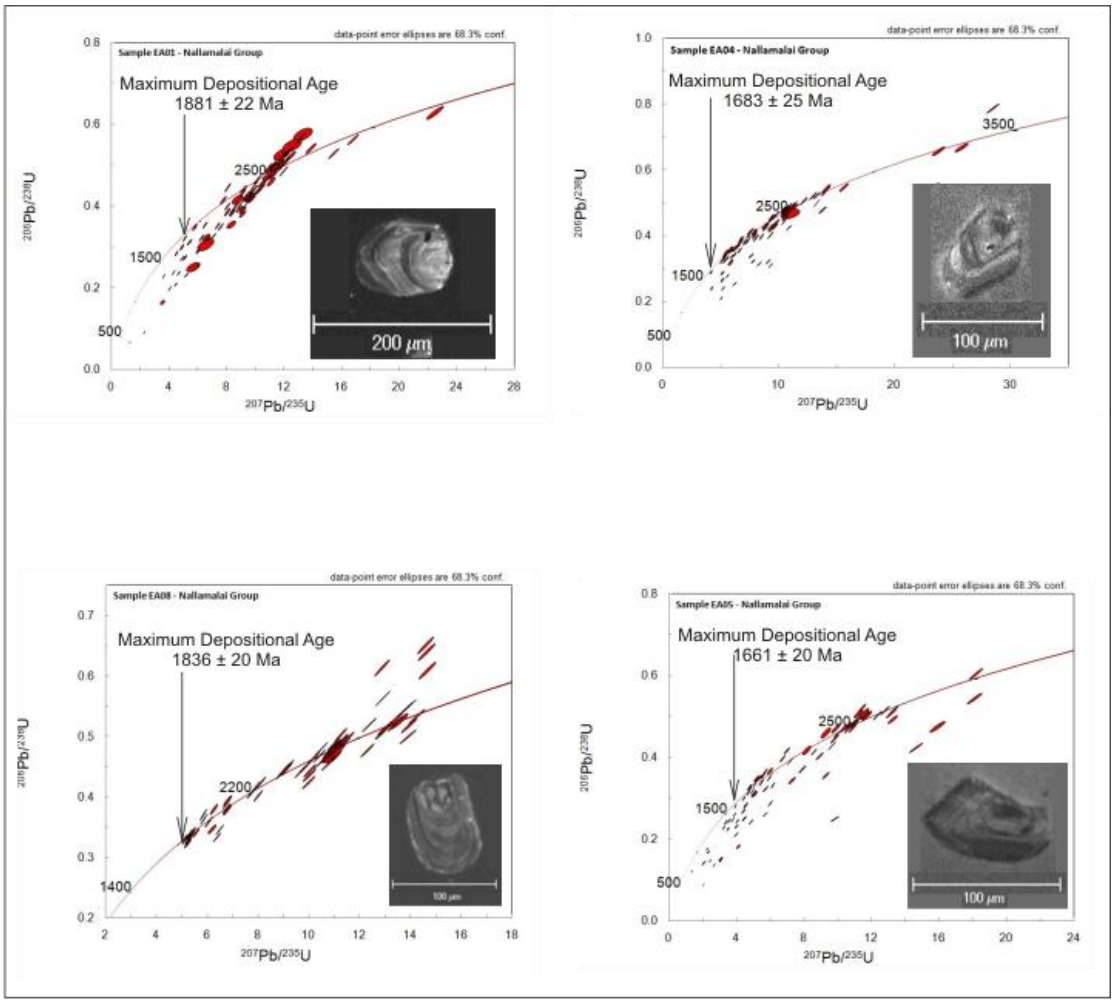
data-point error ellipses are 68.3% conf.
Sample EA01 - Nallamalai Group
Maximum Depositional Age
1881 ± 22 Ma
2500
1500
500
200 μm
$^{207}Pb/^{235}U$
$^{206}Pb/^{238}U$
Sample EA04 - Nallamalai Group
Maximum Depositional Age
1683 ± 25 Ma
3500
2500
1500
500
100 μm
Sample EA08 - Nallamalai Group
Maximum Depositional Age
1836 ± 20 Ma
2200
1400
Sample EA05 - Nallamalai Group
Maximum Depositional Age
1661 ± 20 Ma
2500
1500
500
100 μm

Figure 9

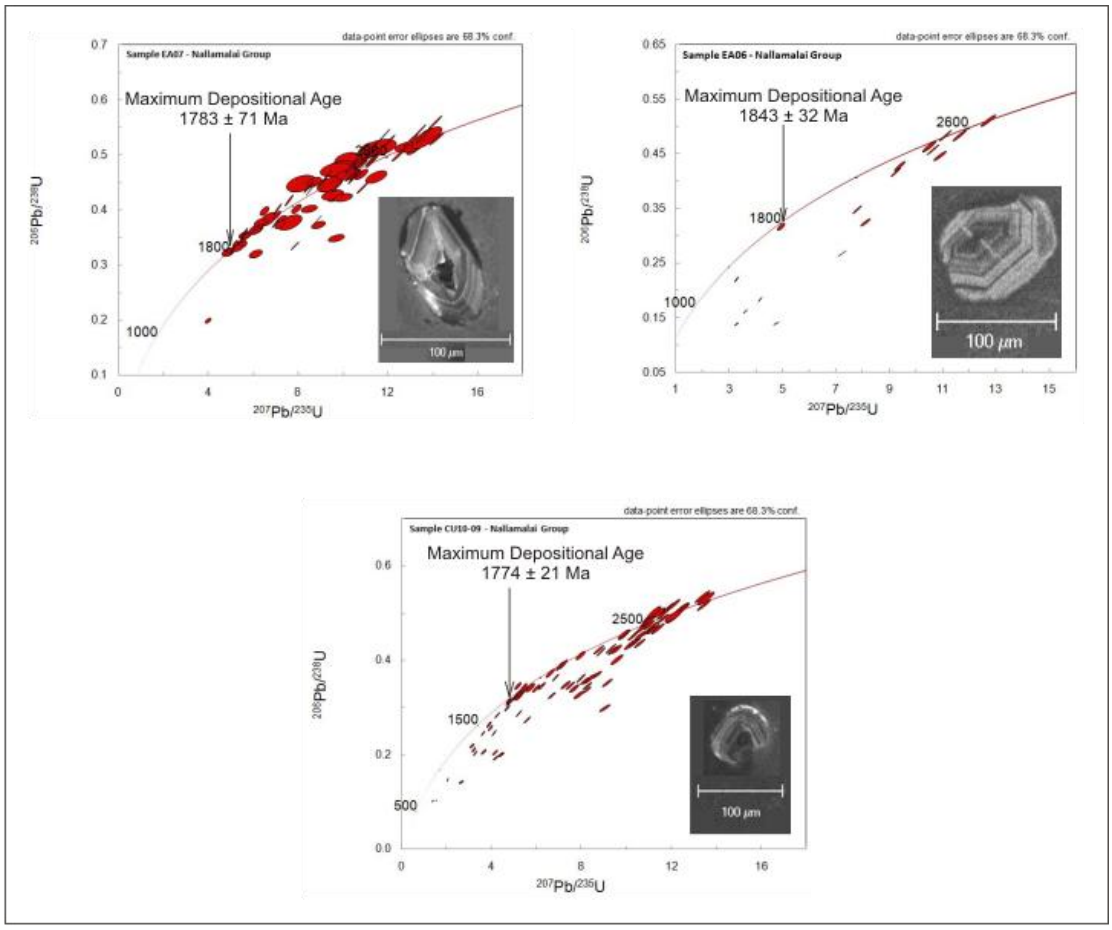
data-point error ellipses are 68.3% conf.
Sample EA07 - Nallamalai Group
Maximum Depositional Age
1783 ± 71 Ma
1800
1000
100 μm
$^{206}Pb/^{238}U$
$^{207}Pb/^{235}U$
data-point error ellipses are 68.3% conf.
Sample EA06 - Nallamalai Group
Maximum Depositional Age
1843 ± 32 Ma
2600
1800
1000
100 μm
$^{206}Pb/^{238}U$
$^{207}Pb/^{235}U$
data-point error ellipses are 68.3% conf.
Sample CU10-09 - Nallamalai Group
Maximum Depositional Age
1774 ± 21 Ma
2500
1500
500
100 μm
$^{206}Pb/^{238}U$
$^{207}Pb/^{235}U$

Figure 10

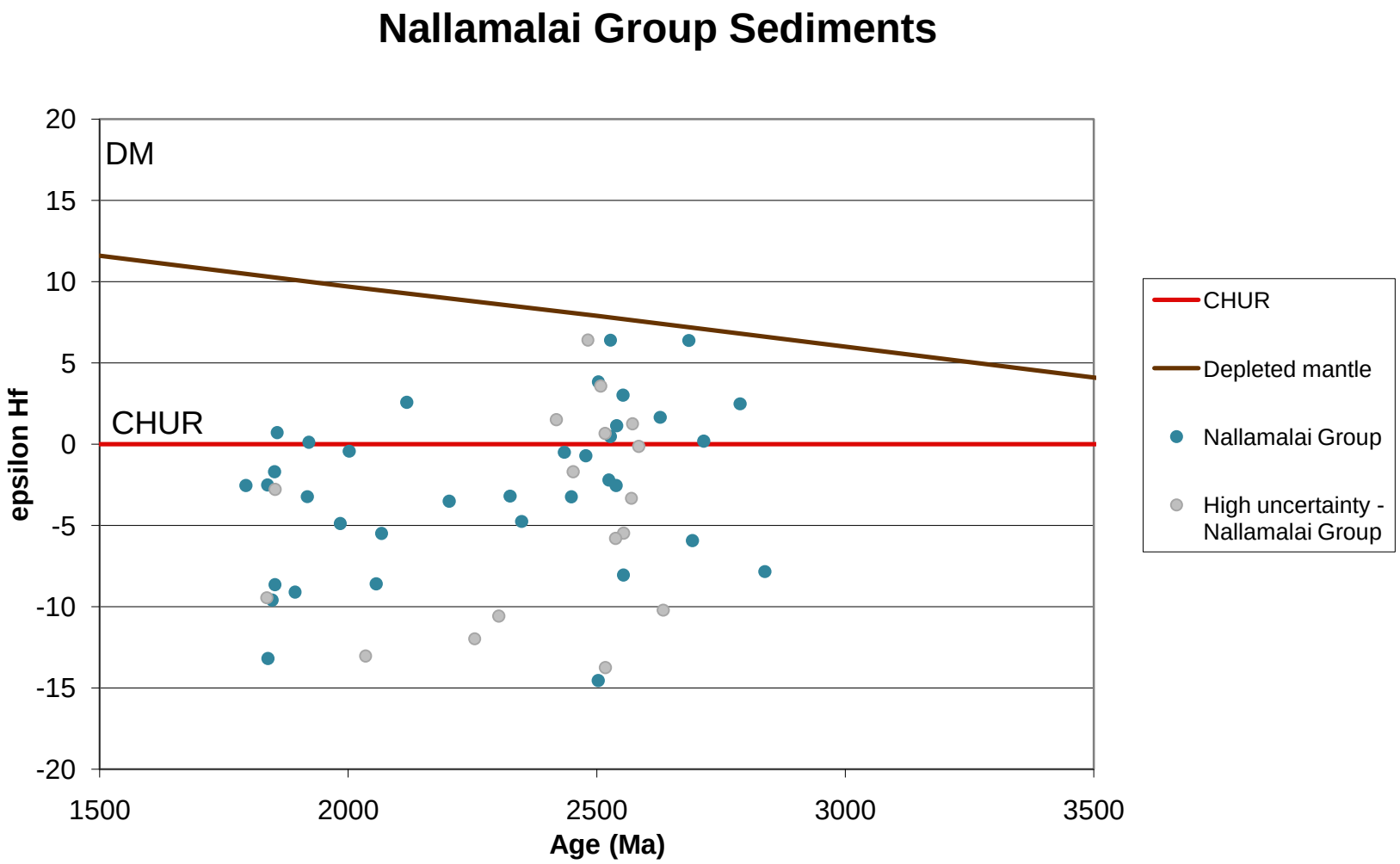
Nallamalai Group Sediments
20
15
10
5
0
-5
-10
-15
-20
DM
CHUR
epsilon Hf
1500
2000
2500
3000
3500
Age (Ma)
CHUR
Depleted mantle
Nallamalai Group
High uncertainty - Nallamalai Group

Figure 11

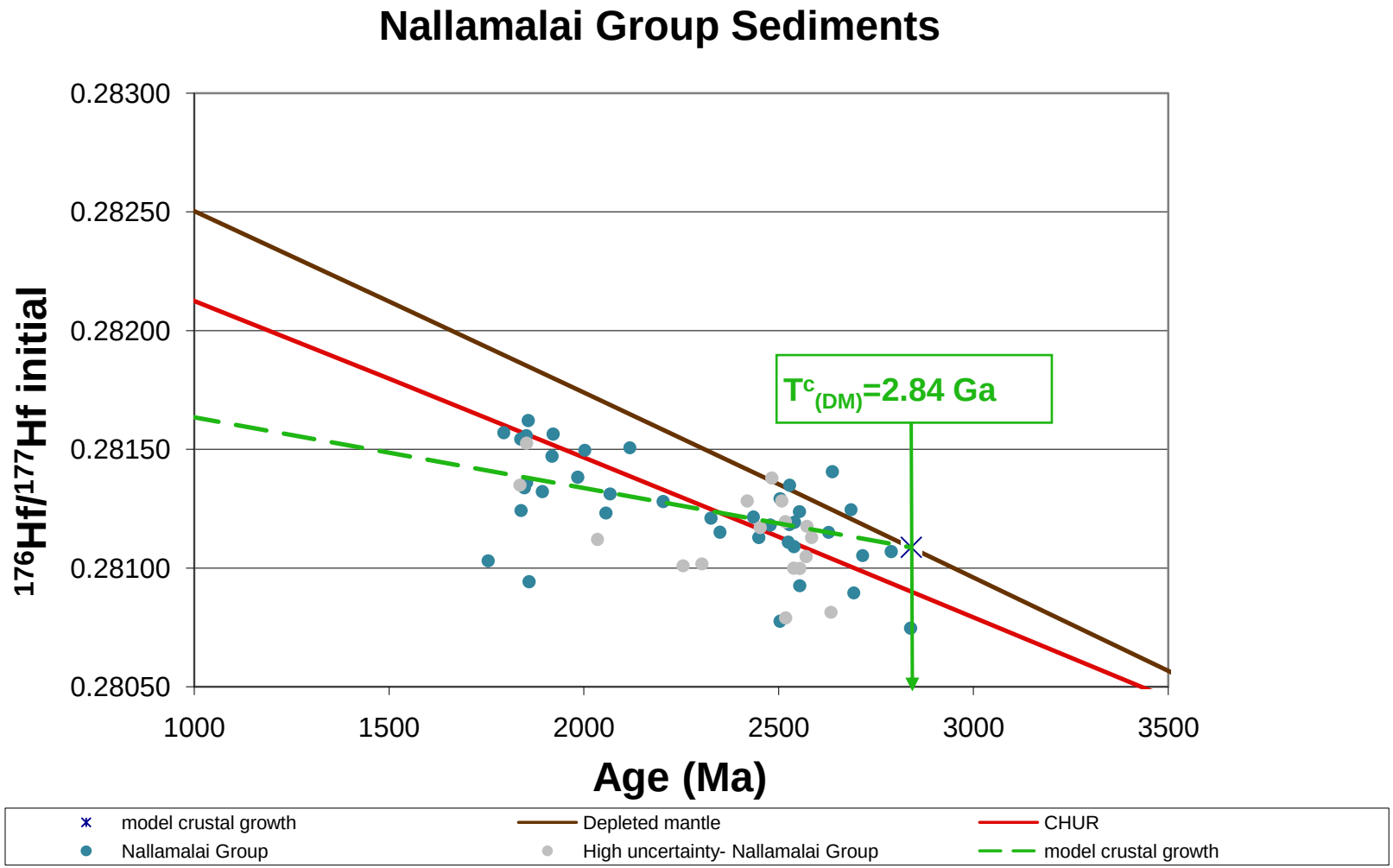
Nallamalai Group Sediments
0.28300
0.28250
0.28200
0.28150
0.28100
0.28050
176Hf/177Hf initial
1000
1500
2000
2500
3000
3500
Age (Ma)
Tc(DM)=2.84 Ga
model crustal growth
Depleted mantle
CHUR
Nallamalai Group
High uncertainty- Nallamalai Group
model crustal growth

Figure 12

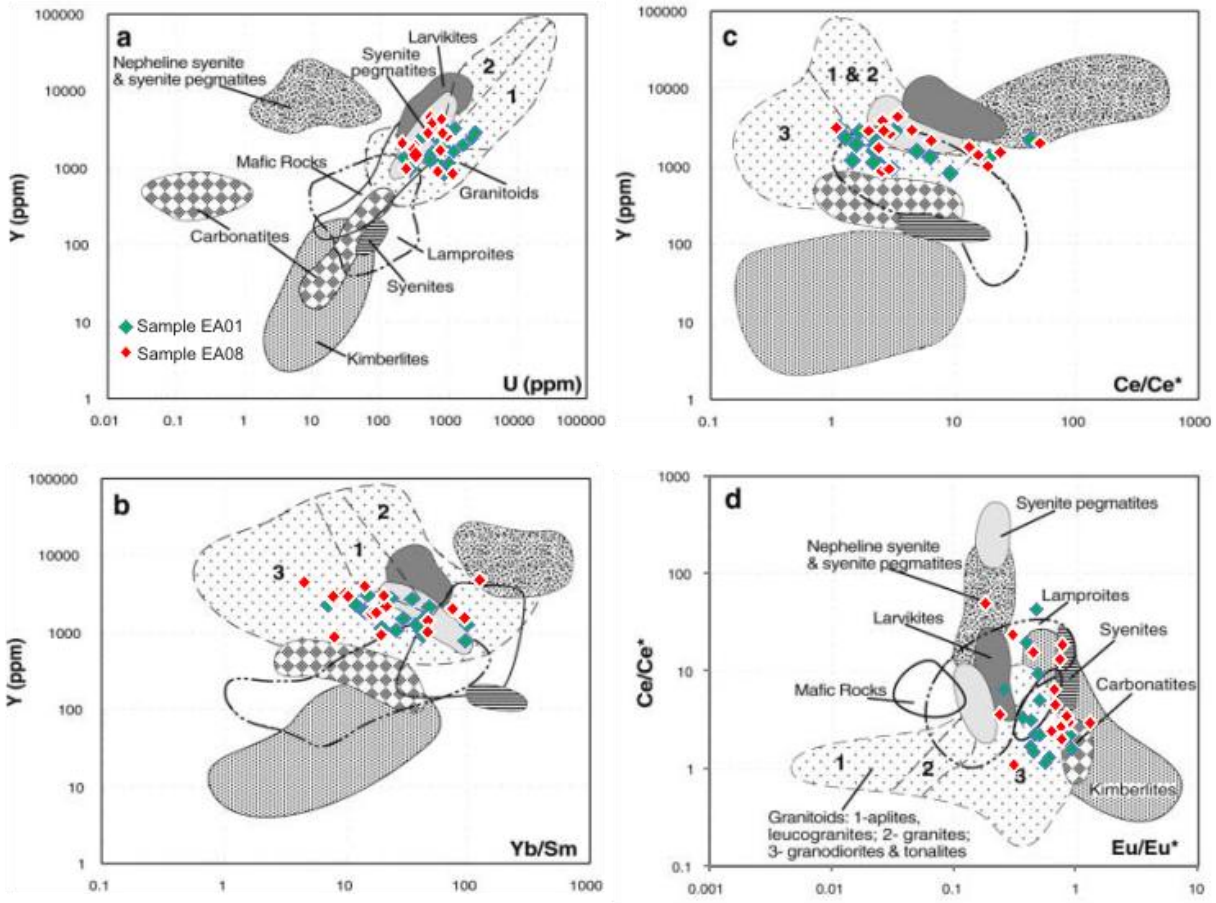
a
Nepheline syenite & syenite pegmatites
Larvikites
Syenite pegmatites
2
1
Mafic Rocks
Granitoids
Carbonatites
Lamproites
Syenites
Sample EA01
Sample EA08
Kimberlites
Y (ppm)
U (ppm)
c
1 & 2
3
Y (ppm)
Ce/Ce*
b
2
1
3
Y (ppm)
Yb/Sm
d
Syenite pegmatites
Nepheline syenite & syenite pegmatites
Lamproites
Larvikites
Syenites
Mafic Rocks
Carbonatites
1
2
3
Kimberlites
Granitoids: 1-aplites, leucogranites; 2- granites; 3- granodiorites & tonalites
Ce/Ce*
Eu/Eu*

Figure 13

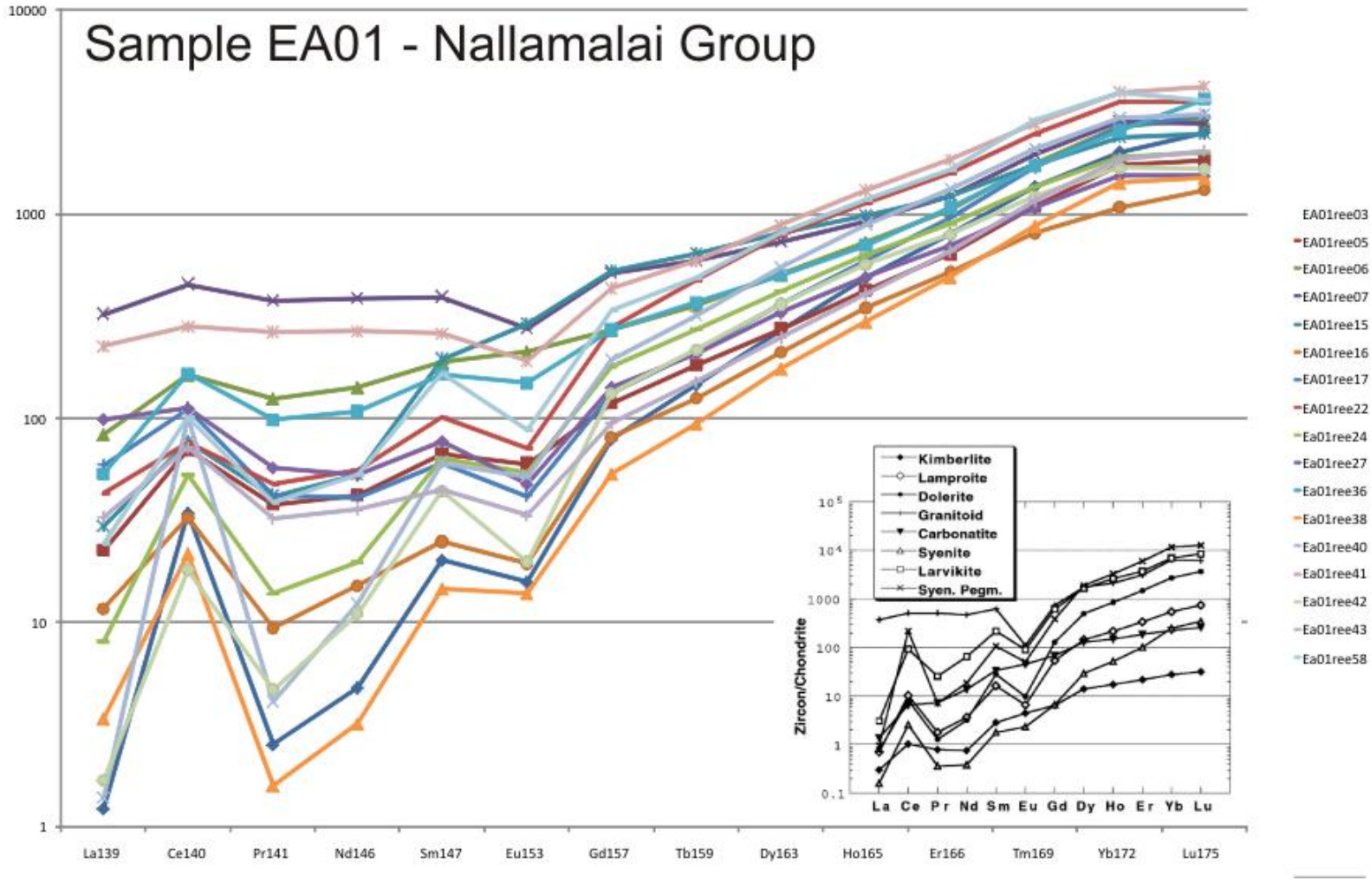
Sample EA01 - Nallamalai Group
10000
1000
100
10
1
La139
Ce140
Pr141
Nd146
Sm147
Eu153
Gd157
Tb159
Dy163
Ho165
Er166
Tm169
Yb172
Lu175
EA01ree03
EA01ree05
EA01ree06
EA01ree07
EA01ree15
EA01ree16
EA01ree17
EA01ree22
Ea01ree24
Ea01ree27
Ea01ree36
Ea01ree38
Ea01ree40
Ea01ree41
Ea01ree42
Ea01ree43
Ea01ree58
Kimberlite
Lamproite
Dolerite
Granitoid
Carbonatite
Syenite
Larvikite
Syen. Pegm.
Zircon/Chondrite
La Ce Pr Nd Sm Eu Gd Dy Ho Er Yb Lu

Figure 14

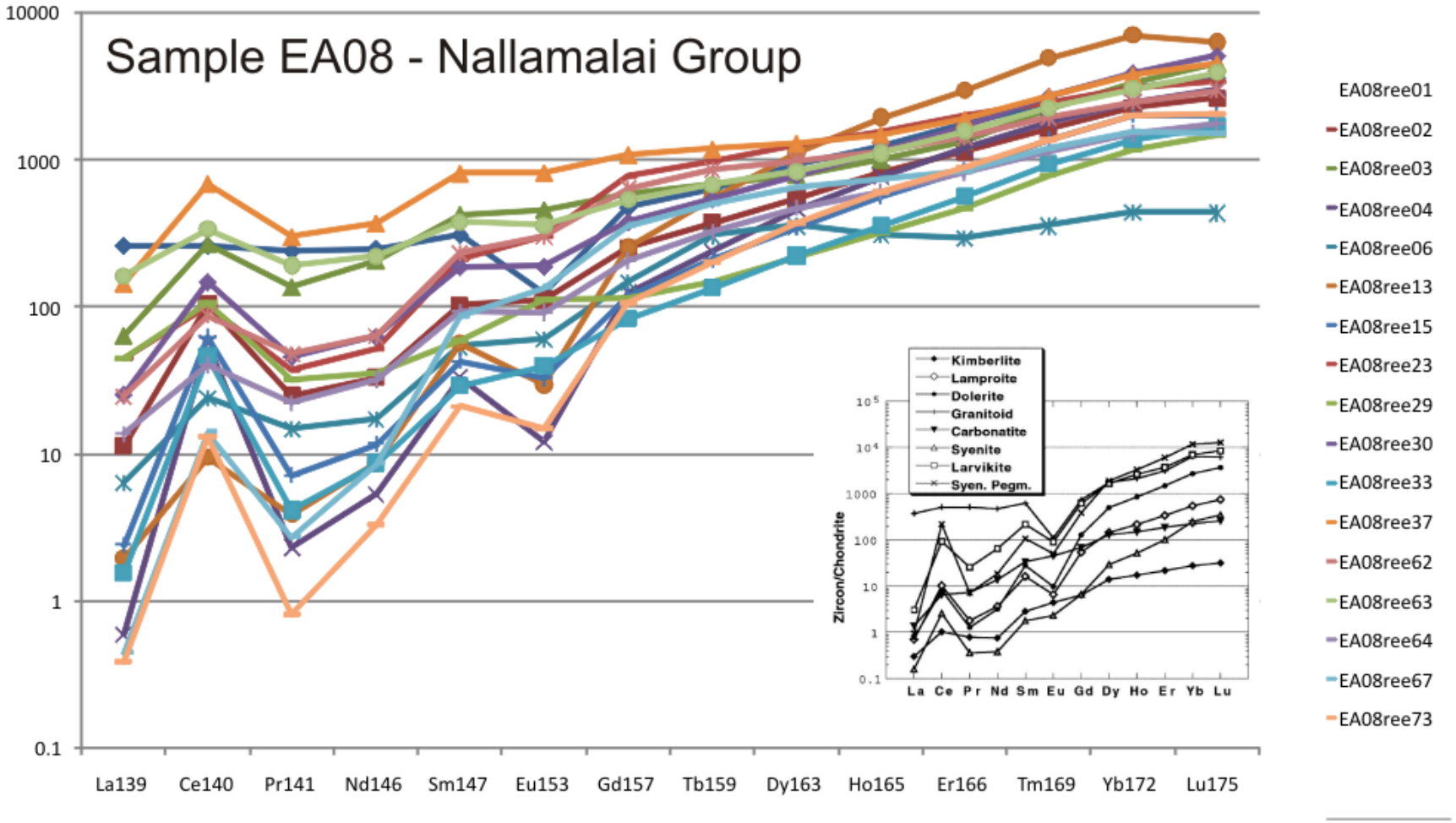
Sample EA08 - Nallamalai Group
10000
1000
100
10
1
0.1
La139
Ce140
Pr141
Nd146
Sm147
Eu153
Gd157
Tb159
Dy163
Ho165
Er166
Tm169
Yb172
Lu175
Kimberlite
Lamproite
Dolerite
Granitoid
Carbonatite
Syenite
Larvikite
Syen. Pegm.
Zircon/Chondrite
La Ce Pr Nd Sm Eu Gd Dy Ho Er Yb Lu
EA08ree01
EA08ree02
EA08ree03
EA08ree04
EA08ree06
EA08ree13
EA08ree15
EA08ree23
EA08ree29
EA08ree30
EA08ree33
EA08ree37
EA08ree62
EA08ree63
EA08ree64
EA08ree67
EA08ree73

Figure 15